Are there reliable methods to estimate the nuclear orientation of Seyfert galaxies?

F. Marin

Monthly Notices
of the
ROYAL ASTRONOMICAL SOCIETY

MNRAS **460,** 3679–3705 (2016)
Advance Access publication 2016 May 12

doi:10.1093/mnras/stw1131

Are there reliable methods to estimate the nuclear orientation of Seyfert galaxies?

F. Marin★

Observatoire Astronomique de Strasbourg, Université de Strasbourg, CNRS, UMR 7550, 11 rue de l'Université, F-67000 Strasbourg, France

Accepted 2016 May 10. Received 2016 May 10; in original form 2016 February 29

ABSTRACT

Together with accretion and evolution, orientation is one of the three main drivers in the grand unification of active galactic nuclei (AGNs). Being unresolved, determining the true inclination of those powerful sources is always difficult and indirect, yet it remains a vital clue to apprehend the numerous, panchromatic and complex spectroscopic features we detect. There have only been 100 inclinations derived so far; in this context, can we be sure that we measure the true orientation of AGNs? To answer this question, four methods to estimate the nuclear inclination of AGNs are investigated and compared to inclination-dependent observables (hydrogen column density, Balmer linewidth, optical polarization and flux ratios within the infrared and relative to X-rays). Among these orientation indicators, the method developed by Fisher, Crenshaw, Kraemer, and others, mapping and modelling the radial velocities of the [O III] emission region in AGNs, is the most successful. The [O III]-mapping technique shows highly statistically significant correlations at >95 per cent confidence level for rejecting the null hypothesis for all the test cases. Such results confirm that the unified model is correct at a scale ranging from kiloparsec to a fraction of a parsec. However, at a radial distance less than 0.01 pc from the central black hole, warps and misalignments may change this picture.

Key words: catalogues – galaxies: active – galaxies: fundamental parameters – galaxies: nuclei – galaxies: Seyfert – galaxies: structure.

1 INTRODUCTION

The question of the geometric properties (positions, orientations and shapes) of cosmic objects concerns every field of astrophysics, from galaxies to gas/dust filaments, binary stars to planet rings, accreting stellar mass black holes to ionized protoplanetary discs (proplyds). To figure out the composition, morphology and kinematics of a source, determining its three-dimensional geometry with respect to the observer is mandatory. It leads to an understanding of complex line profiles such as double-peaked Balmer lines in active galactic nuclei (AGNs; Storchi-Bergmann et al. 1997), the absolute orientation of the binary orbit of extremely massive stars (Madura et al. 2012), or the structure of Keplerian discs around classical Be stars (Carciofi & Bjorkman 2006, 2008). Without measuring and understanding the importance of inclination, dilemma such as the apparent superluminal (faster-than-light) motion in quasi-stellar objects (e.g. Porcas 1983) would still hold. Rees (1966) was the first to predict the possibility of superluminal motion in quasars, a result of high bulk Lorentz factor jets viewed at angles very close to the line of sight (i.e. blazars). This effect has been detected and studied thoroughly since then, and the importance of Doppler orientation bias has been highlighted by Orr & Browne (1982).

Measuring the inclination of the observed target is important but not always easy or direct. The powerful radiation processes occurring in quasars (Mortlock et al. 2011), galaxies (Zitrin et al. 2015)) and gamma-ray bursts (Salvaterra et al. 2009) allow the detection of distant astronomical sources, but their internal structure is almost completely unresolved. Focusing on the most stable emitters (quasars), the host galaxy around their central luminous core may be detected, but the host galaxy's inclination does not necessarily correspond to the inclination of the nucleus (Schmitt et al. 1997). In the nearby Universe, it was found that type 1 AGNs preferentially reside in galaxies seen face-on, but type 2 systems presumably reside in galaxies with a random orientation (Keel 1980; Simcoe et al. 1997; Kinney et al. 2000), even though optically selected type 2 AGN samples tend to avoid edge-on systems (Maiolino & Rieke 1995; Lagos et al. 2011). Historically, it is possible to estimate whether the AGNs we detect are type 1 or type 2 objects through optical classification, the difference relying on the presence/absence of broad Balmer lines in the total flux (Osterbrock 1977). A type 2 AGN lacks those broad emission lines due to dust obscuration along the observer's line of sight; the system is most probably seen at an equatorial viewing angle. Optical polarization measurements successfully confirmed this hypothesis with the detection of broad

★ E-mail: frederic.marin@astro.unistra.fr

Balmer lines in polarized flux, indicating that type 2 Seyfert galaxies are in fact type 1 Seyfert galaxies seen at a specific angle (Miller & Antonucci 1983; Antonucci & Miller 1985), but the exact inclination is almost impossible to determine.

In order to shed light on the growth mechanism of black holes, the physical condition of the early Universe and the formation of galaxies, it is vital to understand the true nature of AGNs, which cannot be achieved without the prior knowledge of how we see them (Shen & Ho 2014). Misclassification of an AGN type can lead to false interpretations of the physics that govern its internal region (Woo et al. 2014). As an example, the presence of equatorial structures around a supermassive black hole (SMBH) can be tested because of their spectroscopic signatures in the X-ray, ultraviolet (UV), optical and near-infrared (NIR) bands. If their geometry is similar to a disc, their observed line emission should be proportional to the cosine of the disc inclination angle with respect to the observer's line of sight (e.g. Wills & Browne 1986). This is a potential method to extract the true inclination of an AGN through its emission-line properties, but we have to be careful as not all emission lines correlate with orientation. The Boroson & Green (1992) eigenvector 1 stipulates that the dominant source of variation in the observed properties of low-redshift quasi-stellar object (QSO) emission lines is a physical parameter that is not always driven by the viewing angle. In particular, the Boroson–Green eigenvector 1 is anticorrelated with the Fe IIλ4570 strength (equivalent width and Fe II/Hβ ratio), anticorrelated with the blue asymmetry of the Hβ line, but correlated with [O III] λ5007 strength (luminosity and peak) and Hβ linewidth.

Thus, it is challenging, but necessary, to estimate the true inclination (with reasonable uncertainty) of Seyfert galaxies and quasars in order to progress beyond the basic assertions of the unified model of AGNs, such as it was proposed by Lawrence (1991), Antonucci (1993) and Urry & Padovani (1995). To achieve this, the identification of a good orientation indicator in quasars is crucial. There are potential indicators to estimate the viewing angle of radio-loud objects (Van Gorkom et al. 2015), such as the radio-core dominance parameter (Orr & Browne 1982), the continuum optical flux density (Wills & Brotherton 1995) or the luminosity of the narrow-line region (NLR; Rawlings & Saunders 1991). However, none of these techniques can be applied to radio-quiet AGNs as they intrinsically miss a relativistic, beamed, parsec-scale jet.

The aim of this paper is to explore the diverse techniques used in the literature to estimate the nuclear inclination of radio-quiet Seyfert galaxies and to identify the best orientation indicator. To achieve this, the catalogue of inclinations used in the sample is described in Section 2, together with the four main Seyfert inclination indicators. The key question is how well a candidate inclination indicator separates the Seyfert 1 galaxies from the Seyfert 2 galaxies. This is investigated in Section 3, where the orientation indicators are compared with inclination-dependent observables. The existence of statistically significant correlations is investigated using efficient rank correlation statistics; the evidence for the unified model is very strong, and while it is not necessary for an inclination indicator to separate the two types perfectly, a near-perfect separation is unlikely to be a coincidence, suggesting a very good indicator. Results and limits are then discussed in Section 4. In Section 5, we conclude the paper by listing the most important outcomes of the comparisons.

2 COMPILING THE CATALOGUE

As the goal of this paper is to achieve a comparison between different orientation indicators, the existence of quantitative evaluations of AGN inclinations is the main driver of the selection process. Only Seyfert galaxies with estimated inclinations were selected, regardless of their redshift, black-hole mass, bolometric luminosity, accretion rate or any spectroscopic features.

2.1 Inclinations from the literature

Roughly 161 AGN inclination values were found during data mining, among which 37 are duplicates. In total, 124 unique radio-quiet objects have an inclination estimation reported in Table A1.[1] This table only accounts for one inclination per AGN; in the case of multiple values, the most probable orientation angle was kept and duplicates were rejected according to two criteria: (i) if the uncertainty of the inclination is larger than 25°, the inclination is discarded as it would cover the whole permitted range of inclination for a given AGN type; (ii) in the case of two different inclinations referring to the same object, the value with the uncertainty encompassing the inclination with less constraint was chosen in order to be conservative. The details of the selected/rejected inclinations are given in Marin (2014).

Almost all these inclination values belong to one of the four main categories of orientation indicators that have emerged while collecting these data. They are classified based on the different mechanisms they use to extract an orientation parameter from their sets of observations and are listed in Tables A2–A5. The duplicates are discussed in Section 4.2, while the four classes of inclination indicators are reviewed in the following subsections. A fifth class, gathering all the inclinations emerging from singular techniques that were employed in isolated papers, is also mentioned for completeness.

2.1.1 *Method I:* M–σ

The M–σ relationship (or $M_{\rm BH}$–σ) is an empirical, significantly tight, correlation between the velocity dispersion σ measured in the bulb of a galaxy and the mass of the SMBH situated at the centre of this galaxy (Ferrarese & Merritt 2000; Gebhardt et al. 2000). In a limited number of AGNs, the SMBH mass can be retrieved using reverberation mapping techniques (e.g. Blandford & McKee 1982; Wandel, Petterson & Malkan 1999; Bentz et al. 2006, 2010), where the mass of the compact source can be estimated from the size of the broad-line region (BLR) and the characteristic velocity of low-ionization, broad, emission lines (LIL, such as Hα, Hβ, Hγ, He I or He II). This velocity, determined by the full width at half-maximum (FWHM) of the emission line, is strongly dependent on the inclination of the BLR. Thus, by assuming a Keplerian motion of the LIL BLR and a similar M–σ relationship between Seyfert 1 galaxies and regular galaxies, Wu & Han (2001) and Zhang & Wu (2002) estimated the orientation angles i for a variety of type 1 AGNs with known black-hole masses and measured FWHM. This resulted in 19 unique inclination estimations, reported in Table A2. Note that the technique, requiring the measurement of the FWHM of low-ionization broad emission lines, is intrinsically limited to type 1 objects.

2.1.2 *Method II: X-ray*

X-ray spectroscopy is a valuable tool that can probe the few inner gravitational radii around a singularity. In AGNs, an accretion disc around the SMBH (Pringle & Rees 1972; Novikov & Thorne 1973;

[1] The tables compiling the various parameters of the sample are given in Appendix A.

Shakura & Sunyaev 1973) acts like a mirror reflecting/absorbing part of the X-ray radiation that is isotropically produced by a hot corona situated above the disc. The corona upscatters thermally emitted, ultraviolet (UV), disc photons to higher energies (Haardt & Maraschi 1991, 1993), producing the observed power-law spectrum. The intense gravitational field around the potential well will affect the re-emitted disc fluorescent emission by broadening the lines due to Doppler effects and gravitational plus transverse redshifts. This will result in a strong asymmetrically blurred emission feature at 6.4 keV, associated with iron fluorescence in near-neutral material (Reeves et al. 2006). Because this fluorescent line is emitted in a disc, its linewidth will be characteristic of the inclination of the system. By applying X-ray spectral fits accounting for a non-Euclidean space–time, it becomes possible to constrain the orientation of the accretion disc, which is usually tied to the AGN inclination (Nandra et al. 1997, 2007). However, this technique is intrinsically limited to bright AGNs. The compilation of X-ray fitted AGN inclination results in 54 unique objects reported in Table A3.

2.1.3 Method III: IR

AGNs act like calorimeters (Antonucci 2012). By absorbing the optical and UV light thermally produced by the accretion disc, the dust embedding the nuclear region will be heated and will re-emit the stored energy at larger wavelengths, principally in the mid-infrared (MIR). The fact that AGNs are surrounded by an asymmetrically distributed amount of dust grains, with a predominance of dust along the equatorial region (the seminal dusty torus[2]), allows a determination of the inclination of the MIR emitting region by looking at the amount of re-emitted radiation and the spectral features in the NIR and MIR spectra (e.g. Mor, Netzer & Elitzur 2009; Alonso-Herrero et al. 2011; Sales et al. 2011; Ruschel-Dutra et al. 2014). To achieve this, clumpy torus models are applied to observed data in order to retrieve several characteristics, such as the spectral energy distribution (SED) or emission and absorption features. Detailed fitting procedures, such as masking the emission lines and the telluric band region (Ruschel-Dutra et al. 2014), or implementing more complex reprocessing geometries (Mor et al. 2009), also help us to better estimate the inclination of the torus. In total, 37 individual objects have been observed and modelled, and the final compilation of inclination values is listed in Table A4.

2.1.4 Method IV: NLR

NASA/ESA *Hubble Space Telescope* (*HST*) observations of the radial velocities of the [O III]-emitting gas in a sample of nearby Seyfert galaxies – for example, NGC 4151 by Crenshaw et al. (2000b) or NGC 1068 by Crenshaw & Kraemer (2000) – have shown that the kinematics of the extended NLR of AGNs tend to be dominated by radial outflows in the approximate morphology of an hourglass. By matching several observed radial velocities to their kinematic model, Crenshaw et al. (2000a) postulated that the orientation of the AGNs could be determined from kinematic mapping. This work was undertaken by Fischer et al. (2013), who used [O III] imaging and long-slit spectra of 53 Seyfert galaxies to extract the inclination of the bicone axis, and hence of the obscuring torus. Using uniform, hollow, bi-conical models with sharp edges, Fischer et al. (2013) found that out of the 53 AGNs they observed, 17 objects had clear enough signatures to retrieve their potential inclination. Those 17 objects are listed in Table A5. Note that, to be able to retrieve an inclination, this technique requires bright, nearby AGNs with resolved NLR structures.

2.1.5 Method V: Other

Under the label 'other' are gathered all the techniques used by a variety of authors to estimate the inclination from one – seldom more – object(s). It includes spectropolarimetric observations and modelling of highly polarized type 1 objects such as ESO 323-G077 (Schmid, Appenzeller & Burch 2003) and Fairall 51 (Schmid et al. 2001), fits of the observed broad, double-peaked Balmer emission lines in NGC 1097 (Storchi-Bergmann et al. 1997) using an eccentric accretion ring model, and several other techniques that are detailed in Marin (2014). The inclinations derived from this mix of approaches are included in Table A1 and contain 25 Seyfert galaxies. As those orientation indicators do not share a common method, the inclinations listed as 'other' will only be used in the global sample.

In total, there are four main indicators: M–σ relationship, X-ray reflection spectroscopy, IR modelling and [O III] mapping. Interestingly, these four methods focus on different and distinct physical scales. In increasing radial distance from the central SMBH: (i) the X-ray method probes the inclination of the inner part of the accretion disc at a couple of gravitational radii (Dovčiak & Done 2016); (ii) the $M0$-σ indicator focuses on the BLR emission, spanning from 10^{-4} to 10^{-1} pc, (Hansen 2014); (iii) the IR method models the dusty torus whose radius is estimated between 10^{-1} and 10^{1} pc (Burtscher et al. 2013); (iv) the [O III] kinematic modelling of the NLR probes physical scales ranging from a parsec up to hundreds of parsec (Crenshaw et al. 2000a). A colour-coded sketch of the unified model is presented in Fig. 1 in order to show the different AGN components targeted by those inclination indicators. It becomes clear that the concept of a global AGN orientation angle is a complicated matter, as the four indicators are meant to measure the inclination of separate components. In the following, the reader is cautioned to remember that the investigations are intended to see if the inclination derived for a given region – X-ray, innermost AGN components; M–σ, BLR; IR fitting, torus; [O III]-mapping, NLR – can be valid over a wider range of physical scales.

2.2 Distribution of inclinations

The final distributions of inclinations are shown in Fig. 2. The top figure presents the histogram of the full sample of 124 Seyfert galaxies, including orientation measurements from all the different methods. The four other histograms show the distribution of inclinations per orientation indicator: middle-left, NLR; middle-right, X-ray; bottom-left, IR; bottom-right, M–σ. Type 1 AGNs are shown in red and type 2 AGNs in green.[3] This graphical ordering and colour-coding will be the same for all the following figures comparing the different inclination indicators.

The distribution of inclinations in the whole sample shows a lack of extreme type 1 objects, as expected from the unified model: if the

[2] The real morphology of the circumnuclear region – compact, clumpy or windy – is not of interest here. The only important characteristic of this obscuring region is that it is close to the equatorial plane.

[3] For the remainder of this paper, it is assumed that Seyfert 1 galaxies show some evidence of a BLR, and therefore all subtypes (types 1, 1.2, 1.5, 1.8 and 1.9) belong to the type 1 category. Type 2s are AGNs without any sign of BLR in total flux spectra.

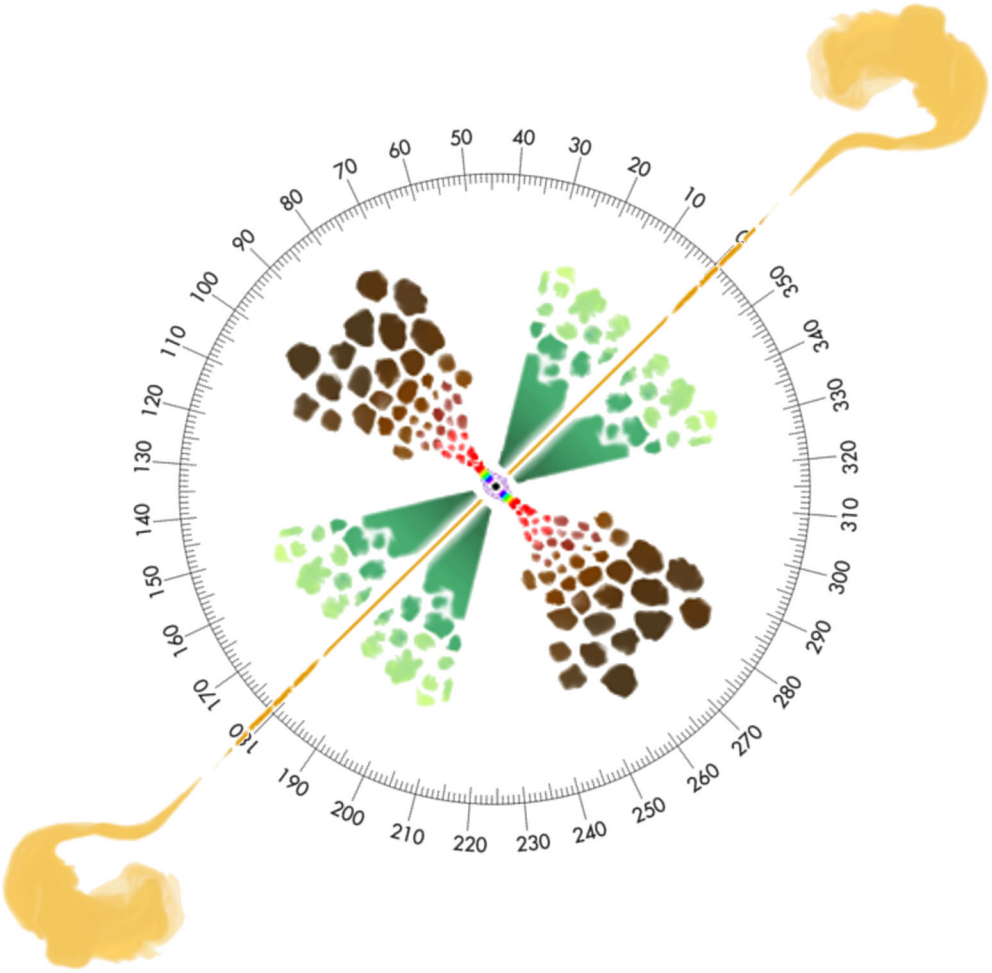

Figure 1. Unscaled sketch of the AGN unification theory. A type 1 AGN is seen at inclinations 0°–60° while a type 2 AGN is seen at 60°–90°, approximately. Colour code: the central SMBH is in black, the surrounding X-ray corona is in violet, the multitemperature accretion disc is shown with the colour pattern of a rainbow, the BLR is in red and light brown, the circumnuclear dust is in dark brown, the polar ionized winds are in dark green and the final extension of the NLR is in yellow-green. A double-sided, kilo-parsec jet is added to account for radio-loud AGNs. Details about the composition and spatial scales are given in the text.

solid angle at which we can detect pole-on AGNs is small, then the observational number count should also be small. The total number of detected sources per solid angle increases with inclination, up to a maximum value at 25°–35°, and the frequency distribution shows a constant diminution until edge-on lines of sight. It appears that the inclinations derived from type 2 Seyfert galaxies do not succeed in filling their solid angle uniformly, otherwise the number count of edge-on AGNs should be higher. This suggests that the inclination indicators might not be suited to retrieve extreme nuclear orientations. Finally, there is only a narrow band of inclinations where type 1 and type 2 AGNs overlap. This range, extending from $i = 36°$ to $i = 72°$, corresponds to the transition region between the two classes of AGNs, where 'changing-look' AGNs[4] are detected (e.g. Elvis et al. 2004; Risaliti et al. 2005; Matt et al. 2009). This range of inclinations is consistent with the type 1/type 2 transition limits (≥45°) found by torus-obscuration modelling of the *INTEGRAL* all-sky hard X-ray survey by Sazonov, Churazov & Krivonos (2015), and is also consistent with optical polarimetric compilation and modelling (Marin 2014), where a transition region between 45° and 60° was found. At first glance, the inclination properties of the global sample are in agreement with past deductions.

Looking at the histograms of the four main orientation indicators, both the IR and M–σ methods are able to reproduce the expected number count of AGNs per solid angle at type 1 inclinations, but the NLR method by Fischer et al. (2013) lacks the statistics to draw any conclusions. The transition region between the obscured and unobscured nuclei is at ∼60° in the case of the NLR method, between 44° and 72° for the X-ray method, and at ∼68° for the IR fitting method. The last orientation indicator, only targeting type 1 AGNs, gives a lower limit of 62°. Overall, the four methods agree relatively well.

2.3 Summary of the inclination-independent characteristics of the sample

The AGN selection process, purely based on the existence of an orientation indicator, results in a final catalogue that might be biased with respect to some intrinsic properties. While not directly

[4] Changing-look AGNs are characterized by rapid variation in the line of sight of cold absorber. These eclipses, mostly observed in X-rays, suggest that these absorbers are located on compact scales consistent within the inner wall of the torus, the BLR and the outer part of the accretion disc, and seen at a line of sight that is grazing the circumnuclear obscuring dust.

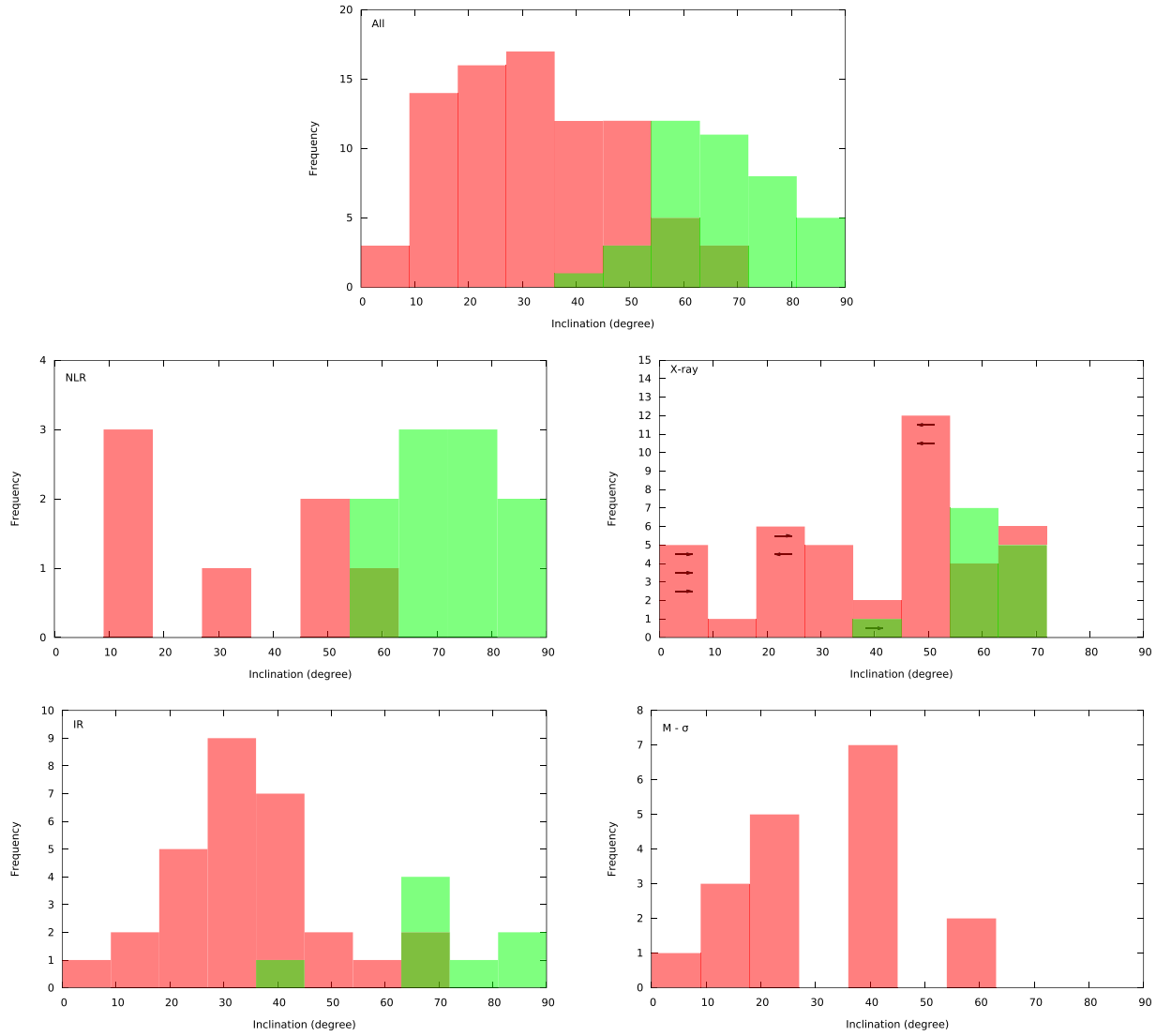

Figure 2. Frequency distributions of AGN inclinations according to the method used to retrieve the nuclear orientation. The top histogram is the cumulated histogram of all methods, minus inclinations that did not pass the selection criteria. Middle-left, NLR method; middle-right, X-ray method; bottom-left, IR method; bottom-right, M–σ method. Type 1 and type 2 AGNs are in red and in green, respectively. The dark-green colour results from the superposition of both type 1 and type 2 Seyfert galaxies.

related to the topic of inclination of Seyfert galaxies, it is necessary to investigate whether those characteristics are likely to bias the analysis.

2.3.1 *Redshift*

Fig. 3 (top) shows the redshifts of the 124 Seyfert galaxies in the global sample, and the redshifts of the four subcatalogues. Redshifts are taken from the NASA/IPAC Extragalactic Data base (NED),[5] where the parameters for distances and cosmology are $H_0 = 73.0$ km s^{-1} Mpc^{-1}, $\Omega_{\rm matter} = 0.27$ and $\Omega_{\rm vacuum} = 0.73$. It appears that the global sample consists of nearby ($z < 0.33$) AGNs at 94.4 per cent, as well as seven broad absorption-line (BAL) QSOs ($z > 1$). All the Seyfert galaxies investigated within the framework of this paper, looking at four orientation indicators, are closer than $z = 0.35$. Given the relatively close redshift range, cosmological effects (evolution) can be considered as negligible. None of the four AGN subsamples shows significant dependence between inclination and redshift, such as expected from studies of radio-loud quasars (Drouart et al. 2012).

2.3.2 *Black-hole masses*

As almost all the AGNs to be investigated are situated in the nearby Universe, the black-hole mass (which is a fundamental property of AGNs that governs the accretion rate) of the catalogues should not have significantly varied between the different lowest and largest redshifts of this sample. In a sample of 377 radio-quiet and radio-loud AGNs, Woo & Urry (2002) found that the mass distribution is narrow in the case of Seyfert galaxies (with average masses $\sim 10^8$ M$_\odot$), with no black-holes masses greater than 10^9 M$_\odot$. Comparing the sample of 124 objects in this paper with their results (see Fig. 4, top), we also find a sharp cut-off at 10^9 M$_\odot$ and a distribution that peaks at $\sim 10^{7.7}$ M$_\odot$. These conclusions also apply to the

[5] http://ned.ipac.caltech.edu/

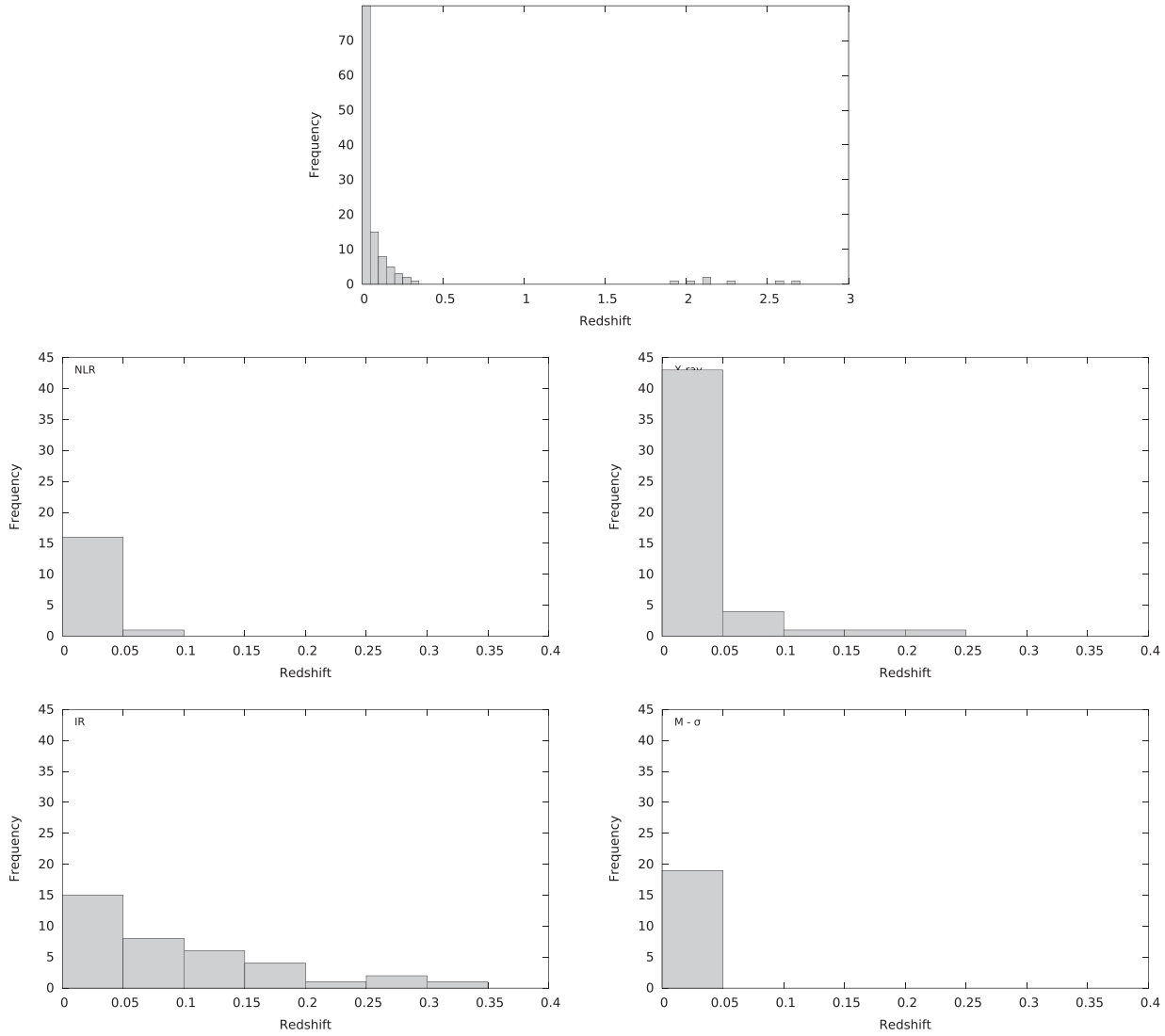

Figure 3. Frequency distribution of the redshifts of the sample. The legend is the same as in Fig. 2.

black-hole masses of the four inclination indicators, which all peak at 10^7 $M_\odot$ < M_{BH} < 10^8 $M_\odot$. These agreements confirm that the catalogues of AGNs used in this paper are not biased either towards light or very massive SMBHs.

2.3.3 *Bolometric luminosities*

The distribution of bolometric luminosities in the global sample (Fig. 5, top) presents a general bell curve centred around log (L_{bol}) = 44.73 (standard deviation = 1.15), the typical signature of a Gaussian distribution. The power output of the 124 AGNs is therefore normally distributed and coherent with the average luminosity of radio-quiet AGN samples (10^{44-45} erg s^{-1}; see Zakamska & Greene 2014 or Comerford & Greene 2014).

Similarly to the global sample, the subcatalogues of the X-ray, NLR and M–σ indicators peak at 44 < log (L_{bol}) < 45, with the exception of the IR fitting technique that peaks at 45 < log (L_{bol}) < 46 – average luminosity log (L_{bol}) = 45.07 and standard deviation = 0.94. Thus, the IR sample is slightly biased towards luminous AGNs. This is due to the inclusion of the Mor et al. (2009) sample of mid- and far-IR selected QSOs and ultraluminous infrared galaxies (ULIRGs) using observations with the *Spitzer Space Telescope* (Schweitzer et al. 2006). The higher power output of the IR sample might increase the resulting torus mass (Mor et al. 2009), might be anticorrelated with the torus covering factor (Mor et al. 2009) or might alter the radial size of the torus inner's wall (Simpson 2005), but it should not change the nuclear inclination of the system. Only a fraction of detected type 1 AGNs versus type 2 objects will vary with higher power outputs, as is observed in Fig. 2 (bottom-left); the averaged half-opening angle of the torus is of the order of 70°.

It is then safe to conclude that the different samples investigated in this paper are not strongly biased towards a characteristic parameter that could theoretically have an effect on this work. It was also confirmed that the sample is not biased by selection effects (in the sense that the different methods would apply to intrinsically different classes of AGNs): each subsample contains narrow- and broad-line Seyfert 1 galaxies (NLS1 and BLS1), and type 1.5, 1.8, 1.9 and type 2 AGNs. The presence of three low-ionization nuclear emission region (LINER) AGNs is not quantitatively enough to tilt the balance towards a specific Seyfert class, and the seven BAL QSOs are only included in the global sample, which is not the main focus of this paper.

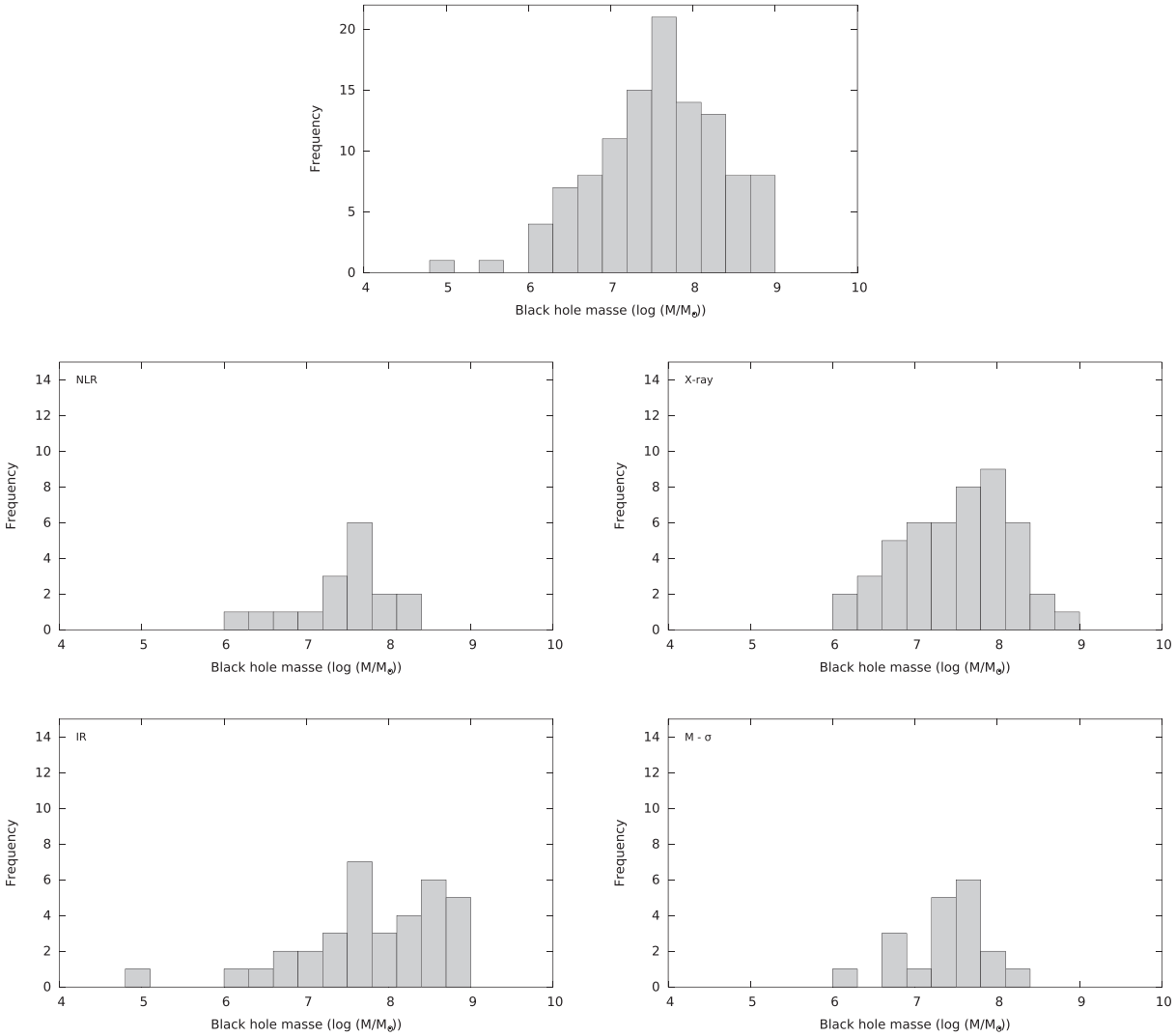

Figure 4. Frequency distribution of the black-hole masses of the sample. The legend is the same as in Fig. 2.

3 CORRELATION WITH MEASURABLE QUANTITIES

In Section 2, four main methods to retrieve the nuclear inclination of Seyfert galaxies have been identified. It is now of prime importance to identify the methods that can be considered as reliable and those that are dubious, in order to improve our fitting and modelling tools. Because the unified model is characterized by a net anisotropy between pole-on and edge-on views, it is logical to expect different observed properties for those two extremes. However, two points of comparison ($\sim$0° and $\sim$90°) are not enough to quantitatively assess the quality of a method. Instead, it is necessary to use multiwavelength observables that are known to vary with inclination. Therefore, the following observable quantities are compared to the different orientation indicators:[6] X-ray column density (Section 3.1), Balmer Hβ linewidths (Section 3.2), optical continuum polarization (Section 3.3) and flux ratios (Section 3.4).

[6] Note that the best way to properly test the reliability of each method would be to compare the same list of objects with inclinations derived by each of the four indicators. However, this is hampered by the fact that only NGC 3227 and 4151 have an orientation estimation evaluated from the four methods.

3.1 X-ray column density

According to the unified model (Lawrence 1991; Antonucci 1993), most of the obscuring material around AGNs is concentrated close to the equatorial plane. This obscuring region presents very high column densities at edge-on views ($n_{\rm H} \gg 10^{24}$ cm^{-2}; Matt et al. 2004b), and the amount of hydrogen does not deviate strongly from a Compton-thick state until the observer's line of sight starts to graze the circumnuclear dust horizon. The lower column density of obscuring material allows the partial transmission of type 1 characteristics such as broad optical lines – for example, Fairall 51 (Smith et al. 2002) or 3C 68.1 (Brotherton et al. 1998) – indicating that the system is seen at an intermediate inclination. The resulting hydrogen column density is in the range $10^{23} \leq n_{\rm H} \leq 10^{24}$ cm^{-2} (Risaliti et al. 2005), a range that corresponds to the changing-look AGN class mentioned in Section 2.1. At inclinations closer to the pole are ionized outflows with low ($n_{\rm H} \leq 10^{23}$ cm^{-2}) hydrogen column densities (Wilkes et al. 2013). However, recent works suggest that $n_{\rm H}$ evolves rather smoothly from the edge to the pole. High-resolution, hydrodynamic, numerical simulations by Wada, Papadopoulos & Spaans (2009) and Wada (2012), looking at the inner parsecs around the SMBH, have recently found that the total gas and H_2

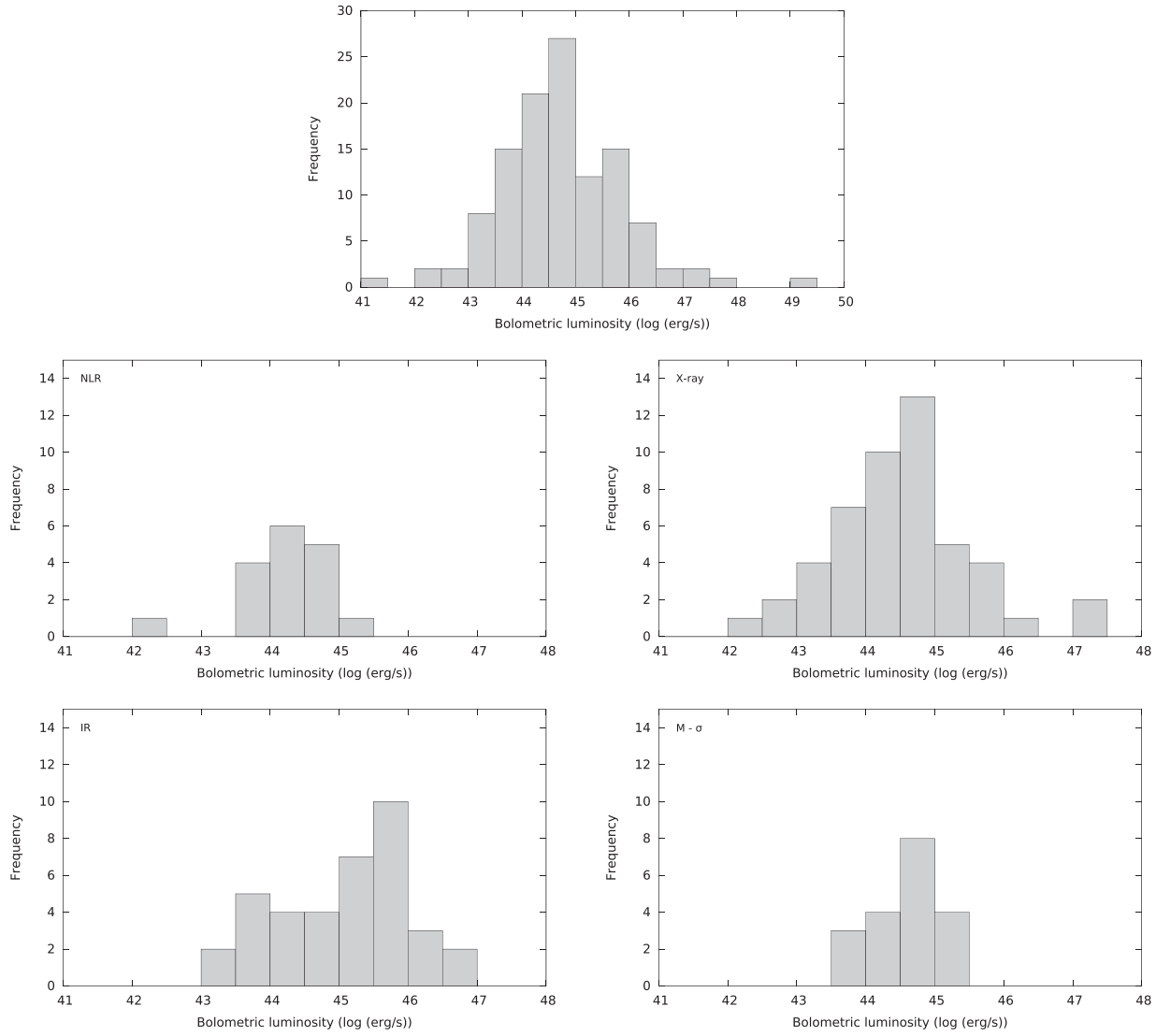

Figure 5. Frequency distribution of the bolometric luminosities of the sample. The legend is the same as in Fig. 2.

column densities evolve smoothly from the Compton-thick equatorial structure to the Compton-thin pole, with the transition angle between the two regimes lying around 50°. According to Wada et al. (2009) and Wada (2012), AGNs are likely to be surrounded by a non-uniform shell of gas with inclination-dependent column densities (see their fig. 4-a). This result is supported by the recent exploration of the correlation between the optical classification of Seyfert galaxies and their observed X-ray absorption by Burtscher et al. (2016). Plotting the estimated X-ray absorbing columns of 25 local AGNs against their Seyfert subclasses (1, 1.5, 1.8, 1.9, 1i, 1h and 2; see Burtscher et al. 2016 for additional information), they found good agreement between optical and X-ray classification, indicating a correlation between i and $n_{\rm H}$.

The collection of intrinsic $n_{\rm H}$ found in the literature is summarized in Table A8, and Fig. 6 presents the different results obtained for the full sample as well as for each orientation indicator. Note that the estimation of hydrogen column densities along the observed line of sight is always model-dependent and potential deviations can be found between two authors. Yet, it clearly seems, as expected, that type 2 AGNs have much higher $n_{\rm H}$ values, with a transition value between type 1 and type 2 AGNs being dependent on the method. There is a large data dispersion in hydrogen column density in all samples, which reflects the diversity of AGNs even at a given inclination (Wada et al. 2009; Wada 2012). Most of the type 2 $n_{\rm H}$ are lower limits, as the procedure for data fitting is often limited to values lower than 10^{25} cm^{-2} due to small signal-to-noise ratios (e.g. Bianchi et al. 2005b) or to computing limitations (e.g. Baloković et al. 2014). Nevertheless, it is possible to look for correlations within the different samples using statistical rank correlation tests (Spearman 1904), while accounting for upper and lower limits (LaValley, Isobe & Feigelson 1992). There are two efficient estimators used to measure the relationship between rankings of different ordinal variables: the Spearman's rank correlation coefficient ρ and the Kendall non-parametric hypothesis test τ for statistical dependence. By normal standards for the sample sizes presented in this paper, a $|\rho|$ value between 0 and 0.29 represents an absence of association, $|\rho|$ between 0.30 and 0.49 represents a possible correlation and $|\rho| > 0.50$ is a highly significant correlation. Usually, τ has lower values, and high statistical significance is reached when $|\tau| > 0.40$. Note that those thresholds depend on the field of study; the $|\rho| > 0.50$ criterion to reach high statistical significance is the one commonly used in physical and social sciences (Cohen 1988;

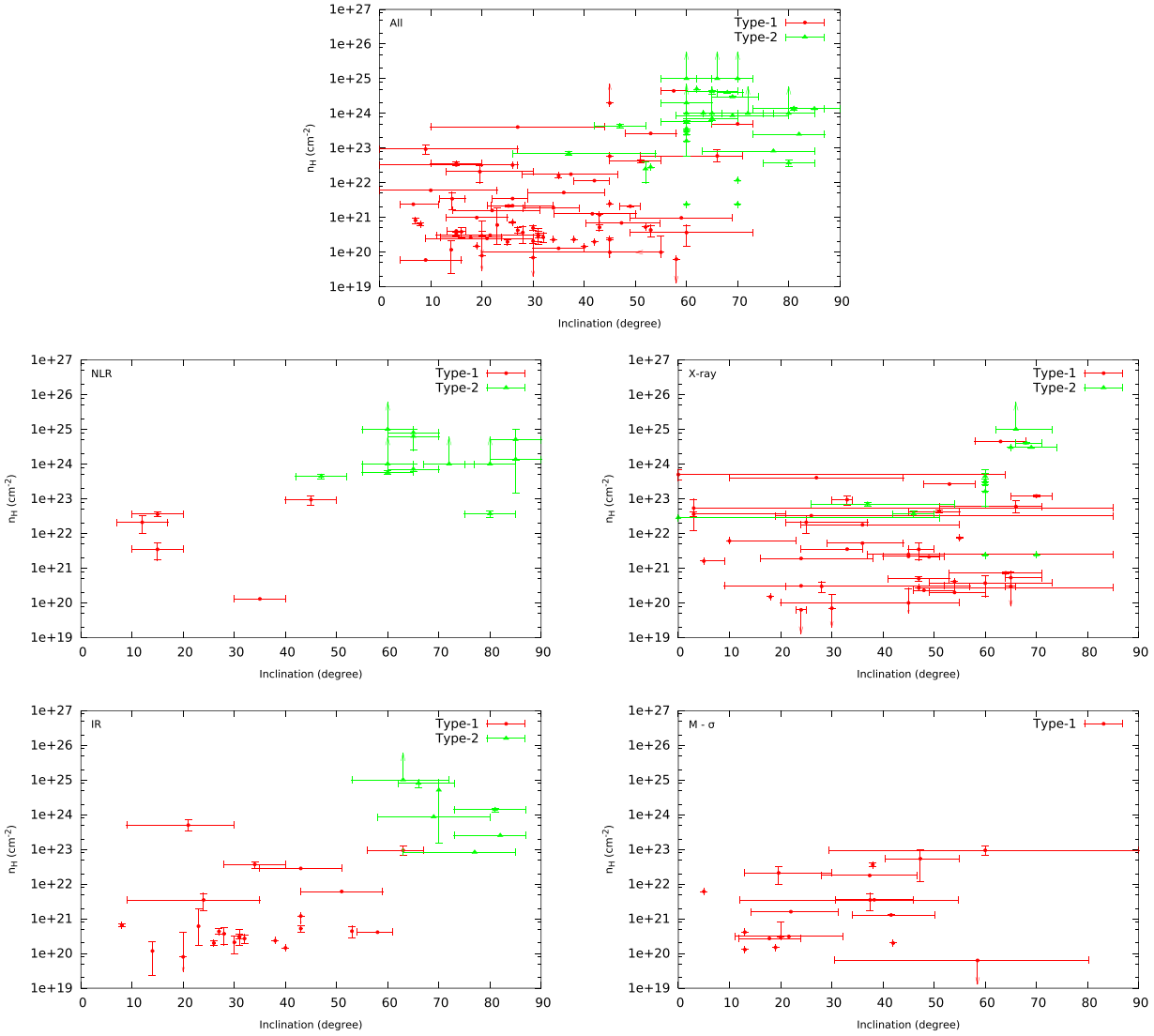

Figure 6. Intrinsic hydrogen column density resulting from X-ray spectral fitting as a function of AGN inclination derived from the indicated method (see text). The legend is the same as in Fig. 2.

Haukoos & Lewis 2005; Curran 2014). The sign of the coefficient indicates whether it is a correlation (positive) or an anticorrelation (negative).

The ρ and τ values for the four inclination indicators, along with their two-tailed p-values, are summarized in Table 1. Both the IR and NLR methods have rank correlation coefficients greater than 0.5, which by normal standards indicates that the association between i and $n_{\rm H}$ is highly statistically significant (at 95 per cent confidence level for rejecting null hypothesis). The X-ray and M–σ methods present weak rank coefficients ($\rho = 0.36$ and $\tau = 0.25$ for the former, and $\rho = 0.31$ and $\tau = 0.26$ for the latter) suggesting a possible correlation. It is interesting to note that, despite being able to reproduce a correlation between inclination and X-ray absorption, the IR, NLR and (possibly) the X-ray methods show very different normalizations. The NLR method suggests that the hydrogen column density is still of the order of 10^{22} cm^{-2} at inclinations close to 10°, while the IR and reflection spectroscopy methods suggest values about two orders of magnitude lower. The former result is high for the unified model standard, as for a Galactic reddening curve, a column density of 10^{22} cm^{-2} corresponds to an extinction in the V band of $A_V = 5$. This can only be explained by a hollow structure of the biconical NLR wind, where the inner funnel is relatively free of gas while the hot flow sustains a much higher column density mixed with dust. The latter methods are more aligned with the predictions of the AGN scheme, where the hydrogen column density would drop to almost zero at perfect polar orientations.

3.2 Balmer Hβ linewidths

There is still debate about the morphology of the region responsible for Doppler broadening of AGN emission lines, directly visible in pole-on quasars but only revealed by scattering-induced polarization in edge-on objects. The discovery of double-peaked Balmer line profiles in a dozen of radio-loud AGNs by Eracleous & Halpern (1994) favours a disc-like geometry dominated by rotational motions. Even more striking evidence comes from the investigation of Wills & Browne (1986), Brotherton (1996) and Jarvis & McLure (2006), who found a highly significant correlation between the ratio of the radio core flux density to the extended radio lobe flux density, R, and the FWHM of broad Hβ lines. The Doppler width

Table 1. Spearman ρ (top) and Kendall τ (bottom) rank correlation coefficients evaluated for the four methods tested in this paper. The values in parentheses are the two-tailed p-values. Cells showing a gray colour are highly statistically significant correlations (at >95 per cent confidence level for rejecting null hypothesis). The number of sources for each sample is indicated in Tables A2–A7.

	NLR	X-ray	IR	M–σ
Spearman correlation ρ				
$n_{\rm H}$ versus i	0.60 (0.02)	0.36 (0.0096)	0.60 (0.00041)	0.31 (0.21)
Hβ FWHM versus i	0.97 (0.0048)	−0.15 (0.38)	0.034 (0.87)	0.44[a] (0.066)
P versus i	0.59 (0.012)	0.28 (0.09)	0.28 (0.092)	−0.14 (0.58)
$F_{2-10\,\rm keV}/F_{25\,\mu\rm m}$ versus i	−0.79 (0.0023)	−0.44 (0.002)	−0.15 (0.51)	−0.11 (0.69)
$F_{6\,\mu\rm m}/F_{25\,\mu\rm m}$ versus i	−0.90 (0.037)	−0.11 (0.60)	−0.17 (0.51)	0.055 (0.88)
Kendall correlation τ				
$n_{\rm H}$ versus i	0.45 (0.02)	0.25 (0.0095)	0.41 (0.0015)	0.26 (0.14)
Hβ FWHM versus i	0.95 (0.043)	−0.11 (0.35)	0.032 (0.83)	0.34[a] (0.053)
P versus i	0.39 (0.038)	0.19 (0.09)	0.16 (0.17)	−0.10 (0.59)
$F_{2-10\,\rm keV}/F_{25\,\mu\rm m}$ versus i	−0.68 (0.0035)	−0.32 (0.003)	−0.13 (0.46)	−0.067 (0.77)
$F_{6\,\mu\rm m}/F_{25\,\mu\rm m}$ versus i	−0.80 (0.086)	−0.11 (0.47)	−0.14 (0.46)	0.022 (1.0)

[a]Biased values (see text for details).

of Balmer lines was found to be unimportant at high R (i.e. when the system is seen close to being face-on). Because Doppler broadening is inclination-dependent, increasing at large viewing angles, the picture is consistent with a disc-like structure of the LIL BLR. However, there is no direct evidence yet that this picture also applies to radio-quiet objects, despite the fact that a small fraction of radio-quiet AGNs also show double-peaked profiles (Marziani, Calvani & Sulentic 1992; Shapovalova et al. 2004). Several authors have tried to reveal this inclination-dependent behaviour using simulations (e.g. Zhang & Wu 2002) even if the width of the point response function at half the maximum intensity remains difficult to estimate due to the observed line variability (Asatrian 2014). As noted by Antonucci et al. (1989), the absence of Lα continuum absorption in any type 1 AGN requires that the clouds producing the broad emission lines are hidden from our line of sight by the circumnuclear region.

Archival optical FWHM measurements of the Hβ λ4861 line were retrieved from the literature for 74 type 1 AGNs. These are listed in Table A7 and plotted against inclination in Fig. 7. The expected relation between the velocity field of the disc-like LIL BLR and the inclination of the system observed by Wills & Browne (1986) in the case of radio-loud AGNs is proportional to $(v_{\rm r}^2 + v_{\rm p}^2 \sin^2 i)^{1/2}$, where $v_{\rm r}$ is a random isotropic velocity and $v_{\rm p}$ is a Keplerian component only in the plane of the disc. According to McLure & Dunlop (2001) and Gaskell & Goosmann (2013), $v_{\rm r}$ is small in comparison with $v_{\rm p}$, and $v_{\rm p}$ is of the order of several thousand km s^{-1}. The expected increase of FWHM with inclination is visible in the plots of the NLR and M–σ methods, as confirmed by the ρ and τ rank correlation coefficients (see Table 1), but the latter method is intrinsically biased. Indeed, Wu & Han (2001) use the Hβ FWHM as a parameter in their equations to retrieve the inclination of their AGN sample (see their equations 2, 3 and 4), so it is logical that there is a good correlation between Hβ FWHM and i. Disregarding the M–σ method from this analysis, only the NLR fitting method by Fischer et al. (2013) is able to retrieve the expected disc-like signature of the LIL BLR (as already shown in Fischer et al. 2014). However, because of the small number of type 1s matched with Hβ FWHM for the NLR technique, additional data are needed to confirm the validity of this correlation. Finally, signs of an anticorrelation between Hβ FWHM and i appeared in the case of the X-ray indicator ($\rho = -0.15$, $\tau = -0.11$), a singular characteristic already mentioned by Nishiura, Murayama & Taniguchi (1998). Such anticorrelation, if real, would indicate that AGNs with face-on accretion discs have larger BLR velocities. This consequence is discussed in Section 4.3.

3.3 Optical continuum polarization

The AGN structure can be probed with great precision by using the geometry-sensitive technique of polarimetry. Optical polarimetry laid the ground for the unified scheme, not only by revealing the predominance of polarization position angles parallel to the projected radio axis of type 1s, while type 2s only show perpendicular polarization position angles (Antonucci 1984), but also by uncovering broad Balmer lines in the polarized flux spectra of type 2 Seyfert galaxies (Miller & Antonucci 1983; Antonucci & Miller 1985). This was one of the strongest assertions in favour of equatorial obscuration, an argument that still holds firmly. By looking at the optical polarization of AGNs, it is possible to estimate the composition, kinematics and geometry of the Seyfert constituents. This has been theoretically and numerically shown in a number of papers (e.g. Kartje 1995; Young 2000; Goosmann & Gaskell 2007; Marin et al. 2012a; Marin, Goosmann & Gaskell 2015), where the linear continuum polarization was found to vary continuously with inclination. The pairing between observed optical polarization measurements and Seyfert types has been examined for a sample of 53 objects in Marin (2014) and this paper will now extend this investigation to a larger number of AGNs, including a diagnostic of the four different methods used to retrieve inclination estimations.

The polarimetric data are listed in Tables A8, A9 and A10, and the plots of optical, continuum, linear polarization P versus inclination i are shown in Fig. 8. In the case of the full sample, there is a clear dichotomy between type 1s and type 2s in terms of polarization degrees, with Seyfert 2 galaxies showing much larger P. However, there appears to be no clear correlation within each individual group. This is particularly relevant for type 1 objects, showing a large P dispersion for a given i. This could result from the competition of parallel (arising from from the accretion flow between the torus and the accretion disc) and perpendicular (from the torus funnel – depending on its half-opening angle – and the polar

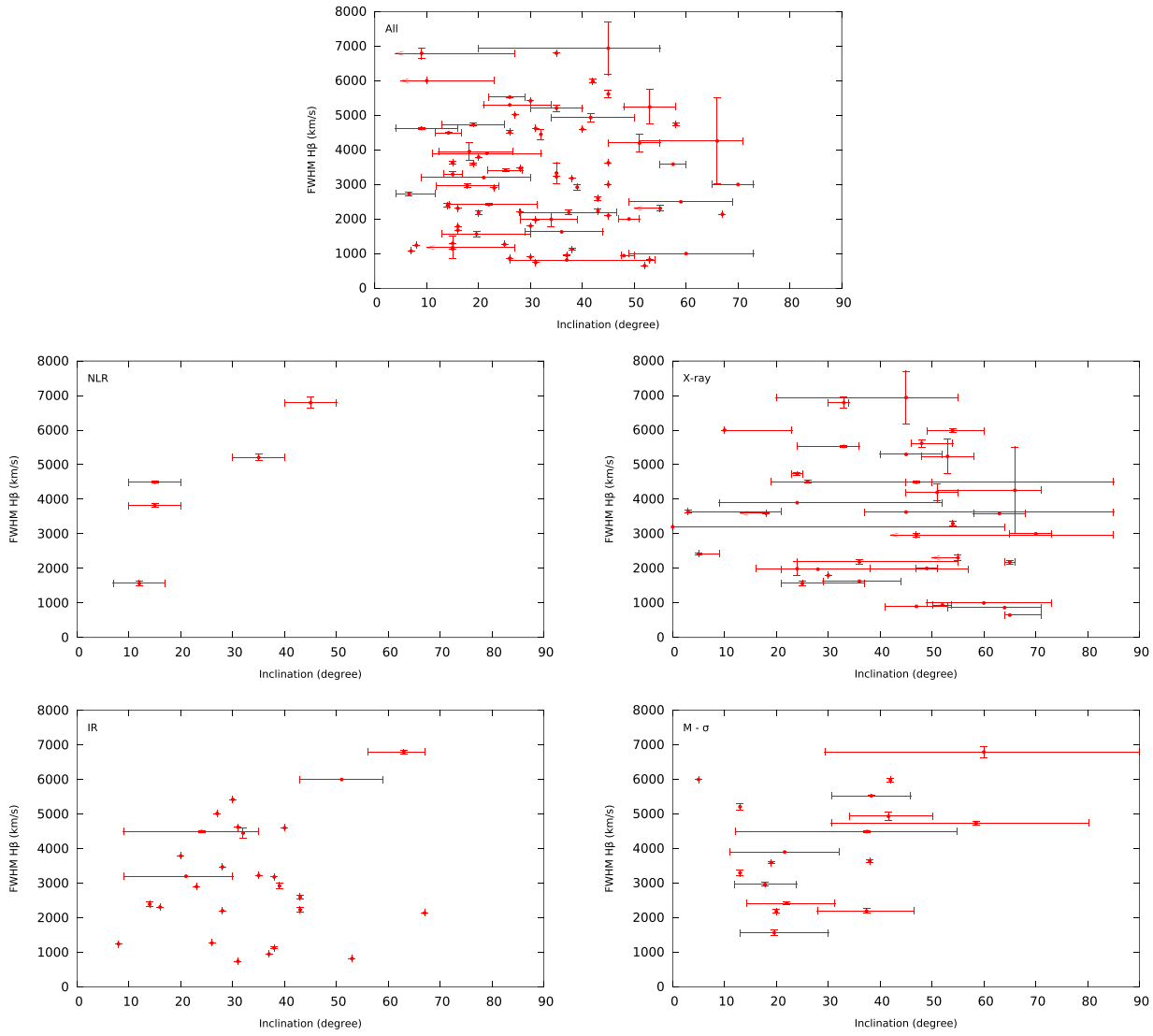

Figure 7. Broad Hβ FWHM as a function of AGN inclination derived from the indicated method (see text). The legend is the same as in Fig. 2.

outflows) polarization components, as type 1s sometimes show perpendicular polarization position angles (Smith et al. 2002). These peculiar objects are called polar scattering dominated AGNs, and are identified and listed in Table A9. The small number of polar scattering dominated AGNs in this sample is unlikely to be the explanation for the dispersion; some of their inclination angles are probably mis-estimated. This appears clearly when plotting P versus i for the four methods: the M–σ method shows no correlation, and the X-ray and IR methods are only weakly correlated ($\rho = 0.28$, $\tau = 0.16$–0.19). The only strong correlation arises from the NLR orientation indicator ($\tau = 0.59$), where P is almost zero at pole-on inclinations, and then rises to about 1 per cent at 20° before decreasing until i reaches ∼40°, where the polarization starts to rise to tens of percent at type 2 inclinations. This behaviour is in excellent agreement with the predictions arising from numerical modelling of the unified scheme. The polarization degree is expected to rise with increasing viewing angles, then to decrease at intermediate orientations, due to the competition between parallel and perpendicular polarizations, and finally to rise again at type 2 angles due to perpendicular scattering in the polar outflows (Marin et al. 2012a, 2015).

3.4 Flux ratios

The anisotropic arrangement of obscuring matter around AGNs, with most of the dust grains and gases located along the equatorial plane, can be used as a strong proxy to estimate whether the object is seen through the circumnuclear dust funnel (pole-on view), or if the radiation is severely obscured (edge-on view). This will result in different fluxes, the former being up to orders of magnitude higher (depending on the waveband considered). However, as stated in Section 3.1, the distribution of matter around AGNs probably varies with inclination, rather than being a binary function, and thus should result in inclination-dependent fluxes. Hence, in the following subsections, two wavebands are investigated to test this hypothesis: the 2–10 keV X-ray and the 6-μm IR fluxes. All fluxes are extracted from the NED (HEASARC) and corrected for redshift.

To normalize the X-ray and NIR fluxes, the *IRAS* 25-μm fluxes were chosen. Based on tight MIR/X-ray correlation, Gandhi et al. (2009) and Asmus et al. (2015) showed that the MIR radiation (at least at 25 μm, as the MIR definition also includes shorter bands) is emitted almost isotropically by dust re-emission; see also Ichikawa et al. (2012) and Hönig et al. (2011) for high-redshift radio galaxies.

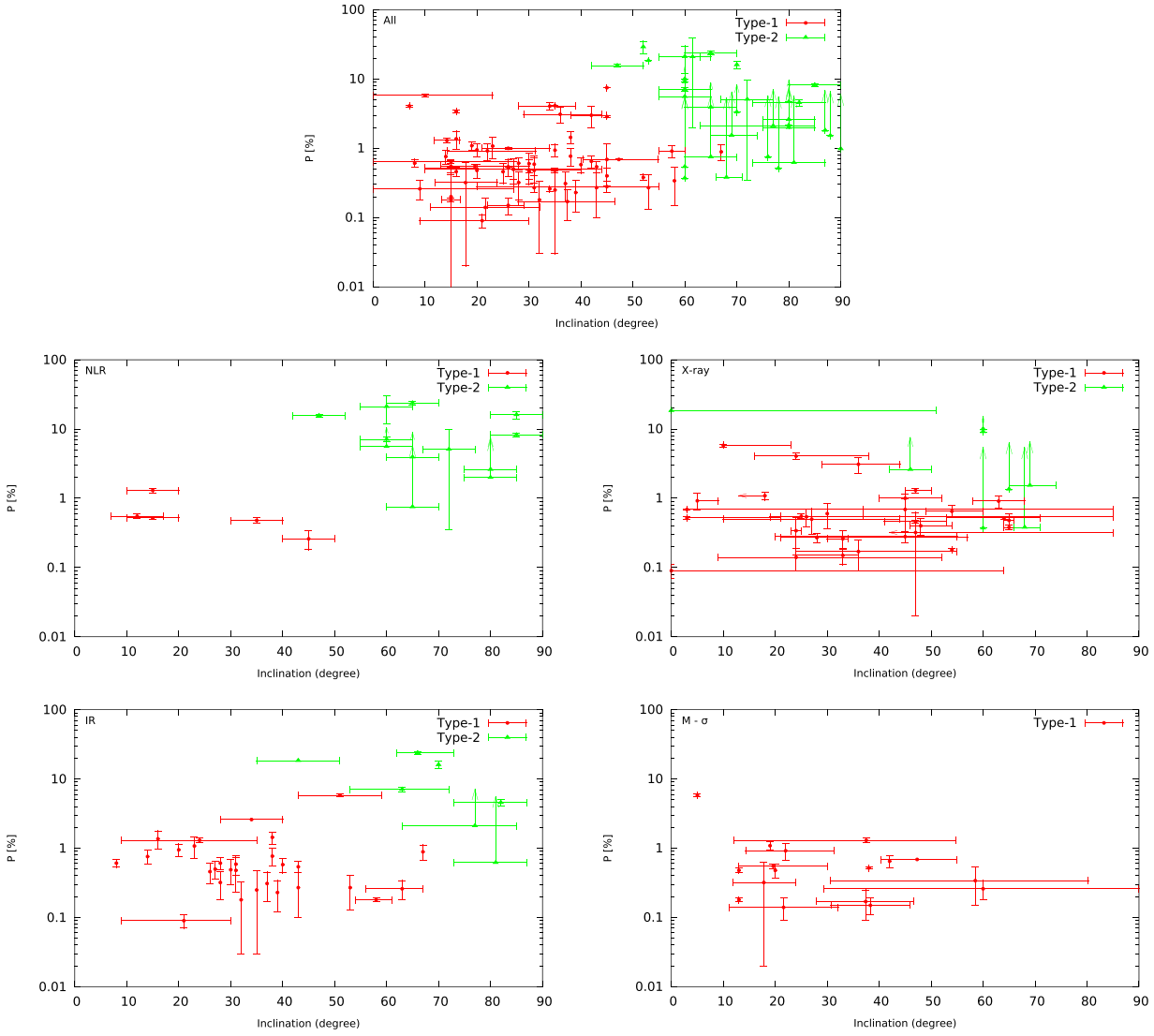

Figure 8. Optical continuum polarization degree P as a function of AGN inclination derived from the indicated method (see text). The legend is the same as in Fig. 2.

The isotropy of MIR emission is supported by interferometric results, where dust re-emission is found to originate not only from the dusty circumnuclear region, but also (and probably predominantly) from the polar outflows (Hönig et al. 2012, 2013; Tristram et al. 2014). In that case, the MIR anisotropy between face-on and edge-on systems is possibly much lower and thus *IRAS* 25-μm fluxes can be chosen as a valid normalization parameter.[7]

3.4.1 XMM–Newton *2–10 keV fluxes*

The X-ray radiation of AGNs is generally thought to result from Compton upscattering of thermal photons in a hot corona. This electron plasma is usually thought to be located in a compact region (a few tens of gravitational radii) above the accretion disc (e.g. Bisnovatyi-Kogan & Blinnikov 1976; Haardt & Maraschi 1991, 1993; Dovčiak et al. 2004; Wilkins & Fabian 2012; Wilkins et al. 2014), which means that the X-ray source is fairly close to the equatorial plane. If the Compton-thick matter that obscures the view of an observer along type 2 inclinations has a height larger than the disc–corona distance, a coplanar observer is thus not likely to see direct X-ray radiation from the corona. The observed X-ray radiation from AGNs is therefore expected to be anisotropic. The 2–10 keV band was selected for the numerous *XMM–Newton* observations that were available in the literature. Harder photons have sufficient energies to pass through the equatorial dust and gas, and softer photons would be too much attenuated by photoelectric absorption by the interstellar and intergalactic media.

As can be seen in Fig. 9, the ratio of X-ray-to-MIR fluxes versus inclination is complicated in the case of the complete sample. Only the most extreme type 2 objects show a net starvation of photons due to equatorial obscuration, and the difference between type 1 and type 2 AGNs is not clear. The same conclusions apply to the IR torus-fitting and M–σ methods, where no correlation is found. The X-ray reflection spectroscopy technique shows a weakly significant anti-correlation ($\rho = -0.44$, $\tau = -0.32$) while the [O III]-mapping indicator clearly stands out. The AGN flux ratio shows a net weakening

[7] Asmus et al. (2015) discuss this result in the context of the torus scenario and present a number of alternatives to explain the MIR emission isotropy.

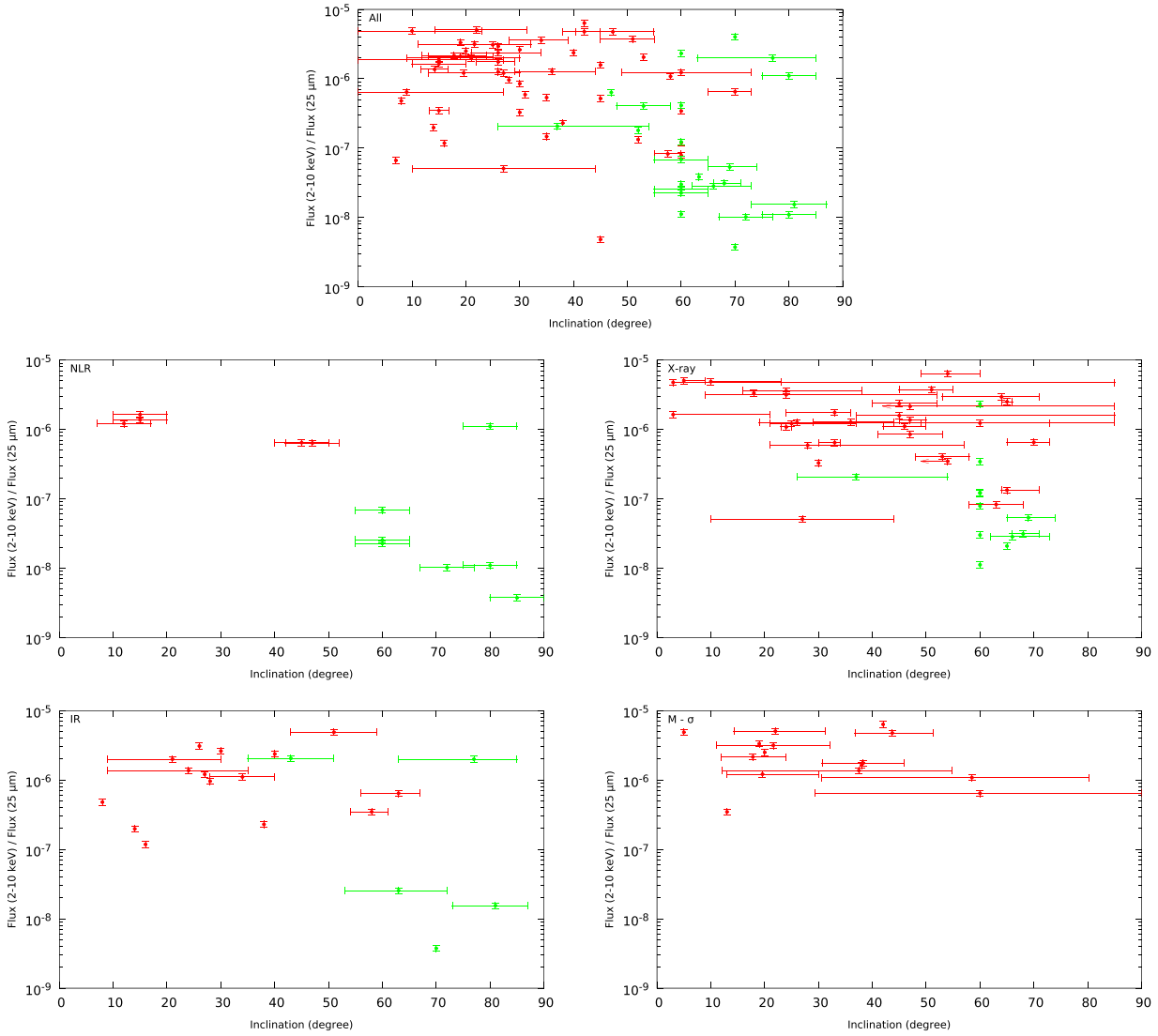

Figure 9. Ratio of the *XMM–Newton* 2–10 keV and *IRAS* 25-μm fluxes as a function of AGN inclination derived from the indicated method (see text). The legend is the same as in Fig. 2.

with increasing inclinations (Fig. 9, middle-left), an anticorrelation supported by large ρ and τ values (-0.79 and -0.68, respectively). There is only one type 2 outsider in this method, NGC 5506, a peculiar case that is discussed in Section 4.1. Between pole-on and edge-on views, the flux ratio differs by a factor of 100, which is consistent with a circumnuclear material with a half-opening angle of 50°–60° with respect to the torus symmetry axis. This threshold value is in agreement with the torus half-opening angles that have been found by Shen, Shao & Gu (2010), Marin (2014) and Sazonov et al. (2015)

3.4.2 Spitzer *6-μm fluxes*

Dust clouds situated at the outer rim of the accretion disc are thought to reradiate the disc emission in the IR band, from 0.5 to a couple of μm (Phinney 1989). At longer wavelengths, isotropic MIR dust re-emission will dominate while the NIR disc signature ends. This effect has been observed by Deo et al. (2009), who have found a deficit of 5.5-μm continuum flux density in Seyfert 2 AGNs with respect to comparable Seyfert 1 AGNs. This confirms the hypothesis that the accretion disc is obscured at type 2 viewing angles and that NIR and MIR flux ratio can be related to the system inclination. This method was used by Fischer et al. (2014) to test the robustness of their inclination predictions, using measurements from *Spitzer*. In this section, the *Spitzer* 6-μm fluxes from the literature are normalized by the *IRAS* 25-μm fluxes for consistency with the previous investigation.

Results are shown in Fig. 10. The flux ratio versus inclination is not conclusive in the case of the full AGN sample, as type 1 and type 2 objects are almost indistinguishable in terms of fluxes. Similarly to Section 3.4.1, the M–σ, X-ray and IR methods fail to show the expected correlation, but the NLR method by Fischer et al. (2013) remarkably stands out. The progressive diminution of flux with inclination is clearly visible and supported by the Spearman and Kendall rank correlation coefficients[8] ($\rho = -0.90$, $\tau = -0.80$;

[8] Despite the limited number of points from the NLR method in the case of the 6-μm/25-μm flux ratio, the Kendall rank correlation and Spearman correlation remain reliable bivariate analyses as they are also adapted to small populations.

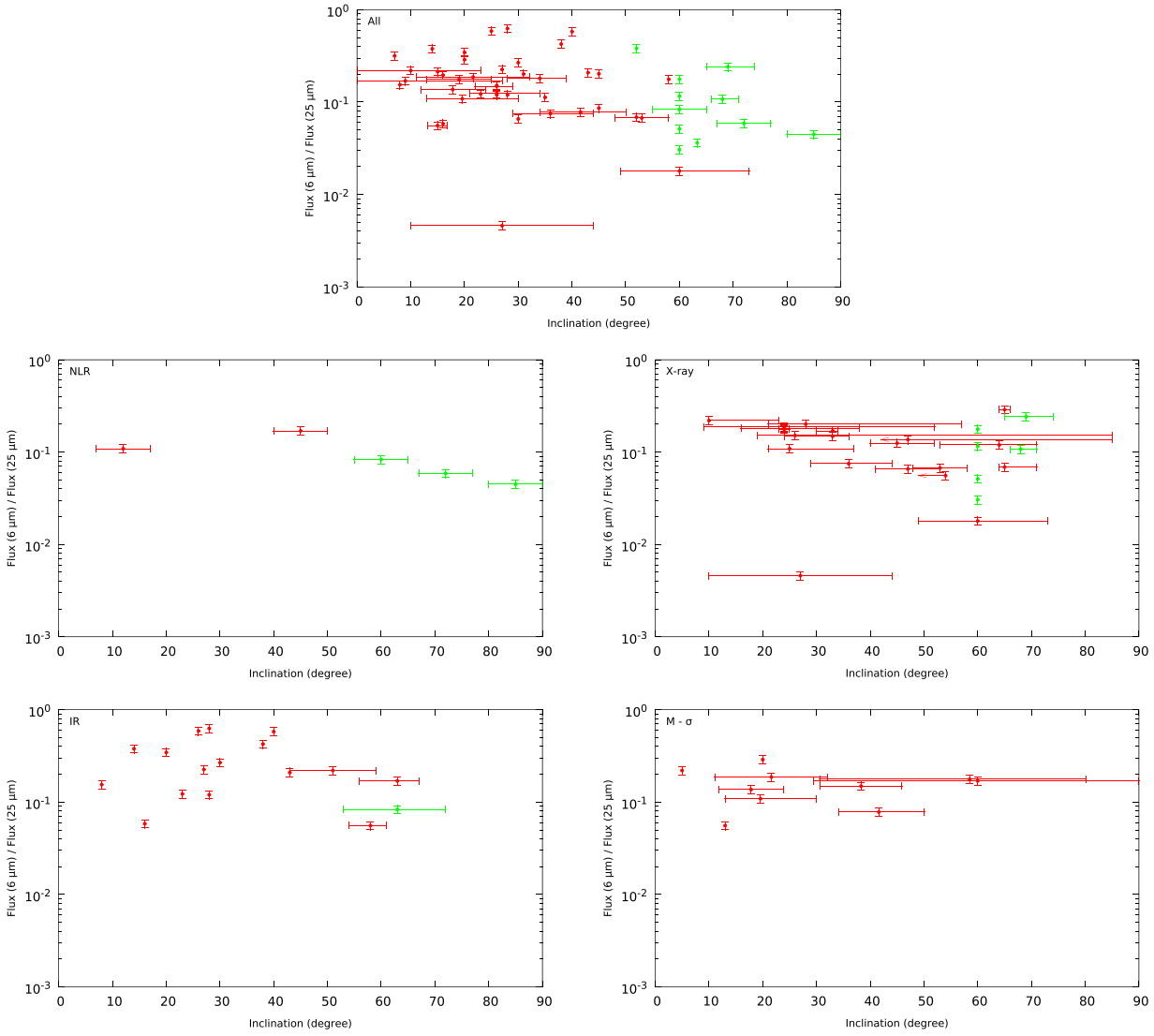

Figure 10. Ratio of the *Spitzer* 6-μm and *IRAS* 25-μm fluxes as a function of AGN inclination derived from the indicated method (see text). The legend is the same as in Fig. 2.

see Table 1). The type 1/type 2 difference is more subtle than in the case of X-ray radiation, as the anisotropic contribution of the outer part of the disc is weak in comparison with the isotropic torus emission that also contributes to the total IR flux. Nevertheless, the inclinations derived by the NLR method are precise enough to reveal the correlation between the IR flux ratio and inclinations.

4 DISCUSSION

4.1 Which one is the best inclination indicator?

The investigations presented in this paper have focused on several inclination-dependent indicators, namely $n_{\rm H}$, Hβ linewidth, optical polarization, $F_{2-10\,{\rm keV}}/F_{25\,\mu{\rm m}}$ and $F_{6\,\mu{\rm m}}/F_{25\,\mu{\rm m}}$, to test the reliability of four techniques (M–σ relation, NLR modelling, X-ray fitting and IR fitting) used to retrieve/estimate the nuclear orientation i of AGNs. Each method focuses on a specific AGN component: the accretion disc in the case of the X-ray method, the dusty torus in the IR fitting technique, the NLR in Fischer et al. (2013) and the internal regions of the host galaxy in the case of the M–σ relation. They are found to have differing reliability. The Spearman and Kendall rank correlation coefficients, presented in Table 1, highlight the valid and invalid indicators.

The method based on the empirical correlation found between $M_{\rm BH}$ and σ by Gebhardt et al. (2000) and Ferrarese & Merritt (2000) proved to be ineffective to reproduce the expected correlations between i and the observed properties. This means that the M–σ relationship, valid for estimating the black-hole mass in non-active galaxies, cannot be applied to AGNs to infer the inclination. The fact that the derived inclinations agree with the mean angle obtained by fitting the iron Kα lines of Seyfert 1 galaxies observed with *ASCA* (Wu & Han 2001) is probably an occurrence based on chance. However, this conclusion does not affect the findings of Xiao et al. (2011) and Woo et al. (2015), who explored the low-mass end of the M–σ relation using narrow-line Seyfert 1 galaxies and found that the NLS1s do not significantly deviate from the expected black-hole mass–stellar velocity dispersion trend, despite an observed offset with the host galaxy morphology.

The X-ray fitting method, taking into account a curved space–time, fails to reproduce the expected inclination-dependent trends at

high statistical significance, though several weak (anti)correlations have been found when looking at dependences between i and $n_{\rm H}$ and $F_{2-10\,{\rm keV}}/F_{25\,\mu{\rm m}}$. A non-isotropically emitting X-ray corona could reinforce the weak correlation between i and $F_{2-10\,{\rm keV}}/F_{25\,\mu{\rm m}}$ (Yang, Wang & Liu 2015), yet none of the evaluated Kendall rank correlation coefficients exceed $\tau = 0.40$, which means that fitting the broad, asymmetric, iron Kα line is not a clear indicator of the global AGN inclination. In particular, measuring the AGN inclination using X-ray spectroscopy is hampered by the fact that the method is biased towards low inclinations: the equivalent width and the reflection fraction decrease with the inclination angle, so highly inclined discs are more difficult to detect (Fabian et al. 2000). Moreover, the larger the inclination, the broader the line, which also plays against detectability.

The third method, based on IR fitting and modelling of the dusty torus, only succeeds in confirming the expected correlation between $n_{\rm H}$ and i at >95 per cent confidence level for rejecting null hypothesis ($\rho = 0.60$, $\tau = 0.41$). This is not surprising as the number density of obscuring clouds is a key parameter in the IR models, and it is used to fine tune the final inclination of the AGN. However, as noted by Feltre et al. (2012), the dust morphology, either smooth or clumpy, has little impact on the modelled SED in modern simulations. Degeneracies may then arise and this would explain why the IR torus modelling fails to reproduce the other inclination-dependent trends (Hönig & Kishimoto 2010). The lack of statistical correlations can also be reinforced by the fact that optical and UV radiation are probably emitted anisotropically, with fewer photons transmitted in the direction closer to the equatorial plane (Kawaguchi & Mori 2010), a feature that is not ubiquitously simulated in all IR models.

It is clear from Table 1 that the method by Fischer et al. (2013), based on kinematic models matching the radial velocities of the [O III]-emitting NLR, is the best inclination indicator tested so far. It succeeded in revealing highly statistically significant correlations (at >95 per cent confidence level for rejecting null hypothesis) between i and $n_{\rm H}$, Hβ FWHM, P, $F_{2-10\,{\rm keV}}/F_{25\,\mu{\rm m}}$ and $F_{6\,\mu{\rm m}}/F_{25\,\mu{\rm m}}$. Fischer et al. (2014) noticed that Mrk 279 and NGC 5506 were almost always outliers in the trends they investigated; the former because column densities from several of its absorbers have yet to be determined, and the latter because the modelled inclination angle is certainly degraded by a highly inclined host disc. The optical classification of NGC 5506 is debated as Goodrich, Veilleux & Hill (1994) found that the Paβ line profile is consistent with the type 2 category, while there is also evidence for permitted O I λ1.1287μm line (with FWHM $<$ 2000 km s^{-1}) and several Fe II lines in the 0.9–1.4 μm spectrum observed by Nagar et al. (2002). Fischer et al. (2013) used the type 2 classification in their paper and several other authors (e.g. Nikołajuk, Czerny & Gurynowicz 2009; Matt et al. 2015) followed the narrow-line Seyfert 1 from Nagar et al. (2002); in our case, removing NGC 5506 from the type 2 category and labelling it as a type 1 would increase the value of the rank correlation coefficients. Using a maximum-likelihood estimation to obtain the best values of ρ and τ from the $n_{\rm H}$ and $F_{2-10\,{\rm keV}}/F_{25\,\mu{\rm m}}$ observables, it is possible to estimate the real orientation of NGC 5506: 40° ± 4°. This value is in agreement with the corrected inclination derived by Fischer et al. (2014): 40°.

The best inclination indicator is thus provided by Fischer et al. (2013), but the necessity to have a well-resolved (distinct knots of emission visible over several arcsec) NLR structure is a major limitation to the method. It constrains the analysis to nearby, bright Seyfert galaxies where long-slit spectroscopy can be applied, but this still represents hundreds of objects (Bennert et al. 2006a,b; Crenshaw & Kraemer 2000; Crenshaw et al. 2000a,b; Fischer et al. 2013). However, it remains unclear how the kinematic model of the authors can account for the changes and misalignments in the polar outflows between the torus and the inner and outer NLR components that have been observed in a couple of AGNs. In the case of NGC 1068, Raban et al. (2009) have noted the misalignment of the *HST*-revealed ionization cone and NLR with respect to the compact and equatorial dust component. Despite lying ∼40 degrees further north from the torus symmetry axis, the observations are still consistent with the kinematic modelling of Das et al. (2006) if the ionized wind is partially obscured by large gas clouds, as suggested by Kishimoto (1999). The question remains open for the treatment of the base of the polar wind, where Müller-Sánchez et al. (2006) located the coronal line region (CLR). The CLR appears to be a medium where forbidden fine-structure transitions in the ground level of highly ionized atoms are responsible for the emission of highly ionized lines. Müller-Sánchez et al. (2011) observed changes between the kinematics of the CLR and NLR for six radio-quiet AGNs, among which the Circinus galaxy, NGC 1068, and NGC 4151 have been analysed by Fischer et al. (2013). The statistically probable inclination derived for those three AGNs indicates that the NLR orientation indicator remains valid at the scales of the CLR, but this needs to be confirmed for the remaining half of the sample of Müller-Sánchez et al. (2011).

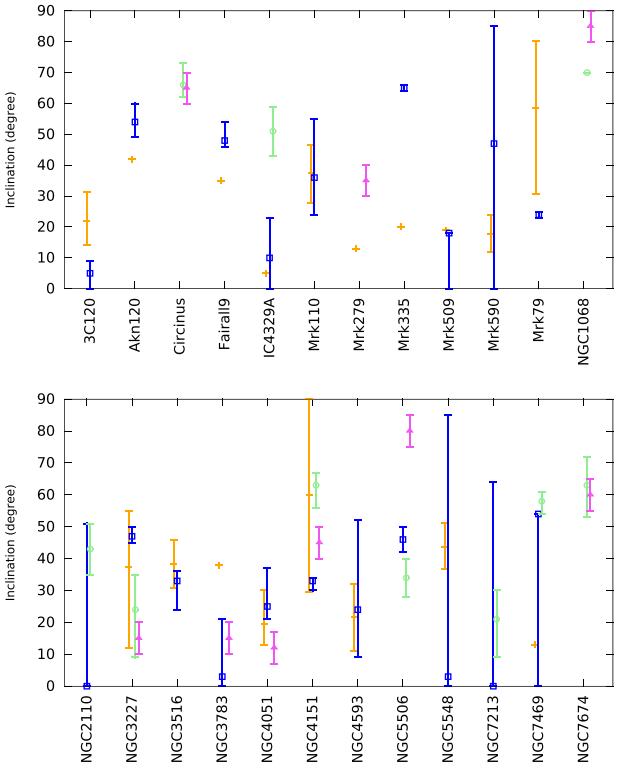

Figure 11. Comparison of the inclination duplicates: M–σ method, orange crosses; X-ray, blue squares; IR, green circles; NLR, pink triangles.

4.2 Orientation duplicates and uncertainty

As stated in Section 2.1, our 124 Seyfert sample takes into account only one inclination per object despite the potential presence of duplicates. However, it has been shown through this paper that the global sample is not reliable. In this case, it is worth investigating if the sample could be fine tuned by selecting more reliable inclinations. Fig. 11 presents the orientation angles for 24 Seyfert galaxies

that have duplicate estimations from at least two different methods. The M–σ approach is marked with orange crosses, the X-ray fitting indicator with blue squares, the IR torus fitting method using green circles and the NLR technique with pink triangles. No dependency between the indicators is found: the angles estimated by Fischer et al. (2013) are not predominantly higher or lower than the angles estimated from another method. In 66 per cent of the cases, the NLR-derived angle is consistent within uncertainty with another technique, but this technique is not always the same. Overall, the data dispersion around the inclinations given by the NLR method shows no trend, and the same conclusion is valid for each of the three remaining methods.

It is interesting to note that the uncertainties retrieved by the 6.4-keV fitting technique are often either very large or unspecified. In this context, it is more difficult to estimate the reliability of the method. The lack of errors is due to the parametrization of the Kerr and Schwarzschild relativistic reflection models, which can be programmed with a fixed inclination. This results in an observer-biased choice that is often set to 30° – e.g. Mrk 509 (Pounds et al. 2001), Mrk 590 (Longinotti et al. 2007), NGC 5548 (Brenneman et al. 2012), NGC 7213 (Ursini et al. 2015) and NGC 7469 (Chiang 2002) – or frozen at 45° – e.g. Mrk 509 (Mehdipour et al. 2011) and NGC 7213 (Emmanoulopoulos et al. 2013) – for type 1 objects. Type 2 inclinations are often set to 60° (e.g. Noguchi et al. 2010). However, if the inclination angle of the disc is left to vary, it will be retrieved by the model using reduced χ^2 statistics to evaluate the goodness of fit. The inclinations found through this less-biased method are almost always dominated by large errors due to the considerable number of free parameters (e.g. Nandra et al. 1997, 2007).

Improving numerical tools is necessary to narrow the uncertainties around the inclination angles derived from X-ray spectral fitting (e.g. Walton et al. 2013; Middleton et al. 2016) and to test, once and for all, the reliability of the X-ray spectroscopic method. In this regard, the help of X-ray polarimetry will be crucial. By fitting the measured spectroscopic and polarimetric information with a unique model (either using reflection spectroscopy or partial covering scenarios; e.g. Iso et al. 2016), the constraints on the nuclear inclination of AGNs will be much stronger as the number of free parameters will be drastically reduced. Information about the disc inclination, the black-hole spin, the luminosity in the thermal flux, and the optical depth, electron temperature and scaleheight of the corona will all become available (Dovčiak et al. 2004, 2011; Schnittman & Krolik 2010; Marin et al. 2012b, 2013).

4.3 Coplanarity within the first parsec

AGNs are usually depicted as axisymmetric structures, where the accretion disc, the BLR and the optically thick equatorial torus are coplanar, and the analyses of this paper have been carried out according to this hypothesis. This is the standard procedure applied by almost every author (e.g. Fine et al. 2008, 2010), but alternative scenarios exist. Pringle (1996) suggested that a powerful radiation source such as the centre of an AGN can modify the dynamics of the accretion disc and induce a warp that could explain the IR emission of Seyfert galaxies. If the equatorial rotating region is subject to a strong outflow, its surface might be even more unstable to warping and lead to detectable signatures in luminous accreting objects that generate energetic winds (Quillen 2001). The idea of twisted accretion discs is not new (Petterson 1977a,b, 1978) but remains little studied despite the observational evidence of warps in maser structures,[9] which are often related to the outer part of accretion discs (Maloney, Begelman & Pringle 1996). If the dense, thin, rotating accretion disc is sufficiently twisted with respect to the BLR or torus region, the inclination estimations produced by fitting the observed X-ray spectroscopic features would only apply to the innermost AGN regions as all the actual models use coplanar, geometrically flat discs. This would explain why the iron Kα fitting method fails to produce reliable global inclinations.

This warping would naturally cause another effect, the non-alignment of the BLR–torus structures with the inner parts of the accretion disc. Bian (2005) already mentioned that the lack of correlation found between the Hβ linewidth measurements and the inclination of the accretion disc derived from X-ray spectral fitting (visible in Fig. 7) seems to indicate that the BLR–torus structures are not coplanar with the accretion disc. A similar conclusion is shared by Nishiura et al. (1998), who additionally found hints of a negative correlation between Hβ and i, which is also what is found in this paper (but with weak rank correlation coefficients: $\rho = -0.15$ and $\tau = -0.11$). They derived a radial distance of 0.01 pc from the central SMBH where the BLR and the outer parts of the disc should be still coplanar. This means that the inclinations derived by the NLR method are valid from kiloparsec scales to a fraction of a parsec, and when the dimensions to be probed meet the inner parts of the accretion disc, another method such as X-ray spectral fitting might become valid.

The situation seems to be the same in radio-loud quasars. Risaliti, Salvati & Marconi (2011) looked at the [O III] equivalent width of thousands of Sloan Digital Sky Survey (SDSS) quasars and reached the same conclusion about the lack of coplanarity between the accretion disc and the circumnuclear absorber. This could be due either to a random alignment between the disc and the torus, or to a very small torus covering factor in the case of quasars. If radio-quiet and radio-loud quasars are similar, with the exception of the jet, then the former hypothesis appears stronger. This is supported by the optical measurements of the polarization position angle of nearby AGNs that almost always deviate from perfect parallel or perpendicular orientation (see, e.g., table 3 in Antonucci 1984). This could be the result from non-coplanar structures within the equatorial dust funnel, but resolution effects must be taken into account as different telescope apertures result in different measurements of the polarization position angle or radio position angle (e.g. Bailey et al. 1988 in the case of NGC 1068).

5 CONCLUSIONS

The conclusions of this paper can be summarized by the following points.

(i) The M–σ relationship, valid for non-active galaxies, cannot be applied to AGNs to retrieve the nuclear inclination.

(ii) Spectral fitting of the AGN SED in the IR band is not a good AGN orientation indicator, except when compared to estimated hydrogen column densities.

(iii) X-ray spectral fitting of the broad and asymmetric fluorescent iron line is too model-dependent and subject to degeneracies to be a valid method to determine the inclinations of AGNs. However, it might work well if the disc is warped by radiation or outflows

[9] Radio observations of NGC 4258 (Miyoshi et al. 1995) and the Circinus galaxy (Greenhill 2000) have revealed that the 22-GHz (1.35 cm) water maser line emission arises from a twisted thin disc that could correspond to the outer rim of the AGN accretion structure.

at small scales, leading to a non-coplanarity of the disc and the BLR–torus structures.

(iv) The method developed by Fischer et al. (2013), based on the original study of Crenshaw & Kraemer (2000), has proven to be very effective in reproducing the expected inclination-dependent signatures of all the observables investigated in this paper. When targeting the extended polar winds, this technique shows that the derived inclination angles are valid at much smaller physical scales (down to a fraction of a parsec where the Balmer line signature originates). This would indicate that this orientation indicator might work on multiple scales, from the extended NLR to the outer parts of the accretion disc. However, the misalignment observed for a few AGNs between the torus and the inner and outer NLR parts might weaken this conclusion.

(v) The expected hydrogen column densities at low inclinations are almost two orders of magnitude larger with the NLR technique with respect to the other orientation estimators. Further detailed observations and modelling are needed to test this method.

(vi) The absence of correlation between the Balmer emission line FWHM and the X-ray-derived inclinations confirms that, if the inclinations are correct, the accretion disc is certainly not co-aligned with the BLR and torus region.

(vii) The orientation of NGC 5506 has been evaluated using the inclination-dependent indicators and corresponds to $40^\circ \pm 4^\circ$.

Additional work is needed in the field of AGNs to understand the structure and the three-dimensional arrangement of the innermost regions of quasars. We plan to try vetting these methods for radio-loud objects using the core dominance parameter, which – at least for high-redshift objects from the Third Cambridge Catalogue of Radio Sources (3CRR) – separates the type 1s from the type 2s perfectly (Marin & Antonucci 2016). Optical polarimetry and [O III] imaging are among the best tools to push forward these analyses, especially when coupled with numerical modelling. Testing the coplanarity (or the absence of coplanarity) between the equatorial structures is mandatory to validate or reject the X-ray spectral fitting method, leading to a potentially strong modification of the unified scheme that would need warped structures at its very centre.

ACKNOWLEDGEMENTS

I would like to acknowledge the anonymous referee for useful suggestions that have helped to clarify this paper. I am also grateful to, in alphabetical order, Robert Antonucci, Michal Dovčiak, René Goosmann, Vladimir Karas, Giorgio Matt, Delphine Porquet, Marvin Rose, Marko Stalevski, Francesco Tamborra, and Belinda Wilkes for their nice comments and helpful suggestions about the results of this work. The Torus2015 Workshop organized by Poshak Gandhi and Sebastian Hoenig was a great mine of information to achieve this work. Mari Kolehmainen was of a great help for English editing. Finally, I am grateful to Jules Garreau (jul.garreau@wanadoo.fr) for his artwork of the various AGN components.

REFERENCES

Agís-González B. et al., 2014, MNRAS, 443, 2862
Alexander D. M., Heisler C. A., Young S., Lumsden S. L., Hough J. H., Bailey J. A., 2000, MNRAS, 313, 815
Alonso-Herrero A. et al., 2011, ApJ, 736, 82
Antonucci R. R. J., 1984, ApJ, 278, 499
Antonucci R., 1993, ARA&A, 31, 473
Antonucci R., 2012, Astronomical and Astrophysical Transactions, 27, 557
Antonucci R. R. J., Miller J. S., 1985, ApJ, 297, 621
Antonucci R. R. J., Kinney A. L., Ford H. C., 1989, ApJ, 342, 64
Arévalo P. et al., 2014, ApJ, 791, 81
Asatrian N. S., 2014, in Mickaelian A., Aharonian F., Sanders D., eds, Proc. IAU Symp. 304, Multiwavelength AGN Surveys and Studies. Cambridge, Univ. Press, Cambridge, p. 407
Asmus D., Gandhi P., Hönig S. F., Smette A., Duschl W. J., 2015, MNRAS, 454, 766
Bailey J., Axon D. J., Hough J. H., Ward M. J., McLean I., Heathcote, S. R., 1988, MNRAS, 234, 899
Baloković M. et al., 2014, ApJ, 794, 111
Barth A. J., Filippenko A. V., Moran E. C., 1999, ApJ, 525, 673
Batcheldor D., Robinson A., Axon D. J., Young S., Quinn S., Smith J. E., Hough J., Alexander D. M., 2011, ApJ, 738, 90
Bauer F. E. et al., 2015, ApJ, 812, 116
Beckmann V., Gehrels N., Favre P., Walter R., Courvoisier T. J.-L., Petrucci P.-O., Malzac J., 2004, ApJ, 614, 641
Bennert N., Jungwiert B., Komossa S., Haas M., Chini R., 2006a, A&A, 459, 55
Bennert N., Jungwiert B., Komossa S., Haas M., Chini R., 2006b, A&A, 456, 953
Bentz M. C., Katz S., 2015, PASP, 127, 67
Bentz M. C. et al., 2006, ApJ, 651, 775
Bentz M. C. et al., 2010, ApJ, 716, 993
Berriman G., Schmidt G. D., West S. C., Stockman H. S., 1990, ApJS, 74, 869
Bhayani S., Nandra K., 2011, MNRAS, 416, 629
Bianchi S., Miniutti G., Fabian A. C., Iwasawa K., 2005a, MNRAS, 360, 380
Bianchi S., Guainazzi M., Matt G., Chiaberge M., Iwasawa K., Fiore F., Maiolino R., 2005b, A&A, 442, 185
Bian W-H., 2005, ChJAA, 5, 21
Bisnovatyi-Kogan G. S., Blinnikov S. I., 1976, SvAL, 2, 191
Blandford R. D., McKee C. F., 1982, ApJ, 255, 419
Boller T., Brandt W. N., Fink H., 1996, A&A, 305, 53
Borguet B., Hutsemékers D., 2010, A&A, 515, A22
Boroson T. A., Green R. F., 1992, ApJS, 80, 109
Brandt W. N., Mathur S., Elvis M., 1997, MNRAS, 285, L25
Brenneman L. W., Elvis M., Krongold Y., Liu Y., Mathur S., 2012, ApJ, 744, 13
Brindle C., Hough J. H., Bailey J. A., Axon D. J., Ward M. J., Sparks W. B., McLean I. S., 1990, MNRAS, 244, 577
Brotherton M. S., 1996, ApJS, 102, 1
Brotherton M. S., Wills B. J., Dey A., van Breugel W., Antonucci R., 1998, ApJ, 501, 110
Browne I. W. A., Murphy D. W., 1987, MNRAS, 226, 601
Burtscher L. et al., 2013, A&A, 558, A149
Burtscher L. et al., 2016, A&A, 586, A28
Carciofi A. C., Bjorkman J. E., 2006, ApJ, 639, 1081
Carciofi A. C., Bjorkman J. E., 2008, ApJ, 684, 1374
Carilli C. L., Wrobel J. M., Ulvestad J. S., 1998, AJ, 115, 928
Chiang J., 2002, ApJ, 572, 79
Chiang C-Y., Walton D. J., Fabian A. C., Wilkins D. R., Gallo L. C., 2015, MNRAS, 446, 759
Chou R. C. Y. et al., 2007, ApJ, 670, 116
Cohen J., 1988, Statistical Power Analysis for the Behavioral Sciences, 2nd edn. Lawrence Erlbaum, Mahwah, NJ
Comerford J. M., Greene J. E., 2014, ApJ, 789, 112
Crenshaw D. M., Kraemer S. B., 2000, ApJ, 532, L101
Crenshaw D. M., Kraemer S. B., 2012, ApJ, 753, 75
Crenshaw D. M. et al., 2000a, AJ, 120, 1731
Crenshaw D. M., Kraemer S. B., Hutchings J. B., Danks A. C., Gull T. R., Kaiser M. E., Nelson C. H., Weistrop D., 2000b, ApJ, 545, L27
Curran P. A., 2014, preprint (arXiv:1411.3816)
Das V., Crenshaw D. M., Kraemer S. B., Deo R. P., 2006, AJ, 132, 620
Dauser T. et al., 2012, MNRAS, 422, 1914
Deo R. P., Richards G. T., Crenshaw D. M., Kraemer S. B., 2009, ApJ, 705, 14
Done C., Jin C., 2016, MNRAS, preprint (arXiv:1506.04547)

Dovčiak M., Done C., 2016, Astron. Nachr., 337, 441
Dovčiak M., Bianchi S., Guainazzi M., Karas V., Matt G., 2004, MNRAS, 350, 745
Dovčiak M., Muleri F., Goosmann R. W., Karas V., Matt G., 2011, ApJ, 731, 75
Drouart G. et al., 2012, A&A, 548, A45
Edri H., Rafter S. E., Chelouche D., Kaspi S., Behar E., 2012, ApJ, 756, 73
Elvis M., Risaliti G., Nicastro F., Miller J. M., Fiore F., Puccetti S., 2004, ApJ, 615, L25
Emmanoulopoulos D., Papadakis I. E., Nicastro F., McHardy I. M., 2013, MNRAS, 429, 3439
Eracleous M., Halpern J. P., 1994, ApJS, 90, 1
Eracleous M., Hwang J. A., Flohic H. M. L. G., 2010, ApJS, 187, 135
Espey B. R. et al., 1994, ApJ, 434, 484
Esquej P. et al., 2014, ApJ, 780, 86
Fabian A. C., Iwasawa K., Reynolds C. S., Young A. J., 2000, PASP, 112, 1145
Fan Y., 2007, PhD thesis, Technical University of Munich
Feltre A., Hatziminaoglou E., Fritz J., Franceschini A., 2012, MNRAS, 426, 120
Feng H., Shen Y., Li H., 2014, ApJ, 794, 77
Ferrarese L., Merritt D., 2000, ApJ, 539, L9
Fine S. et al., 2008, MNRAS, 390, 1413
Fine S., Croom S. M., Bland-Hawthorn J., Pimbblet K. A., Ross N. P., Schneider D. P., Shanks T., 2010, MNRAS, 409, 591
Fischer T. C., Crenshaw D. M., Kraemer S. B., Schmitt H. R., 2013, ApJS, 209, 1
Fischer T. C., Crenshaw D. M., Kraemer S. B., Schmitt H. R., Turner T. J., 2014, ApJ, 785, 25
Gallo L. C., Miniutti G., Miller J. M., Brenneman L. W., Fabian A. C., Guainazzi M., Reynolds C. S., 2011, MNRAS, 411, 607
Gandhi P., Horst H., Smette A., Hönig S., Comastri A., Gilli R., Vignali C., Duschl W., 2009, A&A, 502, 457
Gandhi P. et al., 2014, ApJ, 792, 117
Gaskell C. M., Goosmann R. W., 2013, ApJ, 769, 30
Gebhardt K. et al., 2000, ApJ, 539, L13
Gilli R., Vignali C., Mignoli M., Iwasawa K., Comastri A., Zamorani G., 2010, A&A, 519, A92
González Martín O., 2008, PhD thesis, University of Granada
Goodrich R. W., 1989, ApJ, 342, 224
Goodrich R. W., Veilleux S., Hill G. J., 1994, ApJ, 422, 521
Goosmann R. W., Gaskell C. M., 2007, A&A, 465, 129
Graham M. J. et al., 2015, Nat, 518, 74
Greenhill L. J., 2000, in Conway J. E., Polatidis A. G., Booth R. S., Pihlström Y. M., eds, EVN Symposium 2000, Proc. 5th European VLBI Network Symposium. Onsala Space Observatory, p. 101
Grupe D., Beuermann K., Mannheim K., Thomas H.-C., 1999, A&A, 350, 805
Guainazzi M., Rodriguez-Pascual P., Fabian A. C., Iwasawa K., Matt G., 2004, MNRAS, 355, 297
Haardt F., Maraschi L., 1991, ApJ, 380, L51
Haardt F., Maraschi L., 1993, ApJ, 413, 507
Hansen P. M., 2014, Ap&SS, 352, 235
Haukoos J. S., Lewis R. J., 2005, Academic Emergency Medicine, 12, 360
Hicks E. K. S., Malkan M. A., 2008, ApJS, 174, 31
Hönig S. F., Kishimoto M., 2010, A&A, 523, A27
Hönig S. F., Beckert T., Ohnaka K., Weigelt G., 2007, in Ho L. C., Wang J-M., eds, ASP Conf. Ser. Vol. 373, The Central Engine of Active Galactic Nuclei. Astron. Soc. Pac., San Francisco, p. 487
Hönig S. F., Leipski C., Antonucci R., Haas M., 2011, ApJ, 736, 26
Hönig S. F., Kishimoto M., Antonucci R., Marconi A., Prieto M. A., Tristram K., Weigelt G., 2012, ApJ, 755, 149
Hönig S. F. et al., 2013, ApJ, 771, 87
Ichikawa K., Ueda Y., Terashima Y., Oyabu S., Gandhi P., Matsuta K., Nakagawa T., 2012, ApJ, 754, 45
Iso N., Ebisawa K., Sameshima H., Mizumoto M., Miyakawa T., Inoue H., Yamasaki H., 2016, PASJ, 68, S27
Jarvis M. J., McLure R. J., 2006, MNRAS, 369, 182
Jiménez-Bailón E., Krongold Y., Bianchi S., Matt G., Santos Lleó M., Piconcelli E., Schartel N., 2008a, MNRAS, 391, 1359
Jiménez-Bailón E., Guainazzi M., Matt G., Bianchi S., Krongold Y., Piconcelli E., Santos Lleó M., Schartel N., 2008b, Rev. Mex. Astron. Astrofis. Conf. Ser., 32, 131
Kartje J. F., 1995, ApJ, 452, 565
Kartje J. F., Königl A., Hwang C-Y., Bowyer S., 1997, ApJ, 474, 630
Kaspi S., Smith P. S., Netzer H., Maoz D., Jannuzi B. T., Giveon U., 2000, ApJ, 533, 631
Kawaguchi T., Mori M., 2010, ApJ, 724, L183
Kawamuro T., Ueda Y., Tazaki F., Terashima Y., 2013, ApJ, 770, 157
Kay L. E., 1994, ApJ, 430, 196
Kay L. E., Magalhães A. M., Elizalde F., Rodrigues C., 1999, ApJ, 518, 219
Keel W. C., 1980, AJ, 85, 198
Kinney A. L., Schmitt H. R., Clarke C. J., Pringle J. E., Ulvestad J. S., Antonucci R. R. J., 2000, ApJ, 537, 152
Kishimoto M., 1999, ApJ, 518, 676
Kollatschny W., Dietrich M., 1997, A&A, 323, 5
Kollatschny W., Zetzl M., Dietrich M., 2006, A&A, 454, 459
La Mura G., Berton M., Ciroi S., Cracco V., Di Mille F., Rafanelli P., 2014, Advances in Space Research, 54, 1382
Lagos C. D. P., Padilla N. D., Strauss M. A., Cora S. A., Hao L., 2011, MNRAS, 414, 2148
Laha S., Guainazzi M., Dewangan G. C., Chakravorty S., Kembhavi A. K., 2014, MNRAS, 441, 2613
LaValley M., Isobe T., Feigelson E., 1992, in Worrall D. M., Biemesderfer C., Barnes J., eds, ASP Conf. Ser. Vol. 25, Astronomical Data Analysis Software and Systems I. Astron. Soc. Pac., San Francisco, p. 245
Lawrence A., 1991, MNRAS, 252, 586
Lira P., Videla L., Wu Y., Herrero A., Alexander D. M., Ward M., 2013, ApJ, 764, 159
Lohfink A. M., Reynolds C. S., Miller J. M., Brenneman L. W., Mushotzky R. F., Nowak M. A., Fabian A. C., 2012, ApJ, 758, 67
Lohfink A. M. et al., 2013, ApJ, 772, 83
Longinotti A. L., Bianchi S., Santos-Lleo M., Rodríguez-Pascual P., Guainazzi M., Cardaci M., Pollock A. M. T., 2007, A&A, 470, 73
Lumsden S. L., Alexander D. M., Hough J. H., 2004, MNRAS, 348, 1451
MacKenty J. W., Stockton A., 1984, ApJ, 283, 64
McLure R. J., Dunlop J. S., 2001, MNRAS, 327, 199
Madura T. I., Gull T. R., Owocki S. P., Groh J. H., Okazaki A. T., Russell C. M. P., 2012, MNRAS, 420, 2064
Maiolino R., Rieke G. H., 1995, ApJ, 454, 95
Malizia A. et al., 2008, MNRAS, 389, 1360
Maloney P. R., Begelman M. C., Pringle J. E., 1996, ApJ, 472, 582
Marin F., 2014, MNRAS, 441, 551
Marin F., Antonucci R., 2016, ApJ, in press
Marin F., Goosmann R. W., Gaskell C. M., Porquet D., Dovčiak M., 2012a, A&A, 548, A121
Marin F., Goosmann R. W., Dovčiak M., Muleri F., Porquet D., Grosso N., Karas V., Matt G., 2012b, MNRAS, 426, L101
Marin F., Porquet D., Goosmann R. W., Dovčiak M., Muleri F., Grosso N., Karas V., 2013, MNRAS, 436, 1615
Marin F., Goosmann R. W., Gaskell C. M., 2015, A&A, 577, A66
Marinucci A. et al., 2014, MNRAS, 440, 2347
Markowitz A., Reeves J. N., George I. M., Braito V., Smith R., Vaughan S., Arévalo P., Tombesi F., 2009, ApJ, 691, 922
Marquez I., Boisson C., Durret F., Petitjean P., 1998, A&A, 333, 459
Martin P. G., Thompson I. B., Maza J., Angel J. R. P., 1983, ApJ, 266, 470
Marziani P., Calvani M., Sulentic J. W., 1992, ApJ, 393, 658
Matt G., Bianchi S., D'Ammando F., Martocchia A., 2004a, A&A, 421, 473
Matt G., Bianchi S., Guainazzi M., Molendi S., 2004b, A&A, 414, 155
Matt G., Bianchi S., Awaki H., Comastri A., Guainazzi M., Iwasawa K., Jimenez-Bailon E., Nicastro F., 2009, A&A, 496, 653
Matt G. et al., 2015, MNRAS, 447, 3029
Mehdipour M. et al., 2011, A&A, 534, A39
Mehdipour M. et al., 2015, A&A, 575, A22
Middleton M. J., Parker M. L., Reynolds C. S., Fabian A. C., Lohfink A. M., 2016, MNRAS, 457, 1568

Miller J. S., Antonucci R. R. J., 1983, ApJ, 271, L7
Miniutti G., Ponti G., Dadina M., Cappi M., Malaguti G., 2007, MNRAS, 375, 227
Miniutti G., Piconcelli E., Bianchi S., Vignali C., Bozzo E., 2010, MNRAS, 401, 1315
Miyoshi M., Moran J., Herrnstein J., Greenhill L., Nakai N., Diamond P., Inoue M., 1995, Nat, 373, 127
Mor R., Netzer H., Elitzur M., 2009, ApJ, 705, 298
Moran E. C., 2007, in Ho L. C., Wang J-M., eds, ASP Conf. Ser. Vol. 373, The Central Engine of Active Galactic Nuclei. Astron. Soc. Pac., San Francisco, p. 425
Moran E. C., Barth A. J., Kay L. E., Filippenko A. V., 2000, ApJ, 540, L73
Mortlock D. J. et al., 2011, Nat, 474, 616
Müller Sánchez F., Davies R. I., Eisenhauer F., Tacconi L. J., Genzel R., Sternberg A., 2006, A&A, 454, 481
Müller-Sánchez F., Prieto M. A., Hicks E. K. S., Vives-Arias H., Davies R. I., Malkan M., Tacconi L. J., Genzel R., 2011, ApJ, 739, 69
Nagar N. M., Oliva E., Marconi A., Maiolino R., 2002, A&A, 391, L21
Nandra K., George I. M., Mushotzky R. F., Turner T. J., Yaqoob T., 1997, ApJ, 477, 602
Nandra K., O'Neill P. M., George I. M., Reeves J. N., 2007, MNRAS, 382, 194
Nardini E. et al., 2015, Sci, 347, 860
Nikołajuk M., Czerny B., Gurynowicz P., 2009, MNRAS, 394, 2141
Nishiura S., Murayama T., Taniguchi Y., 1998, PASJ, 50, 31
Noguchi K., Terashima Y., Ishino Y., Hashimoto Y., Koss M., Ueda Y., Awaki H., 2010, ApJ, 711, 144
Novikov I. D., Thorne K. S., 1973, in DeWitt C., DeWitt B. S., eds, Black Holes (Les Astres Occlus). Gordon and Breach, New York, p. 343
O'Brien P. T., Page K., Reeves J. N., Pounds K., Turner M. J. L., Puchnarewicz E. M., 2001, MNRAS, 327, L37
Ogle P. M., Cohen M. H., Miller J. S., Tran H. D., Goodrich R. W., Martel A. R., 1999, ApJS, 125, 1
Orr M. J. L., Browne I. W. A., 1982, MNRAS, 200, 1067
Osterbrock D. E., 1977, ApJ, 215, 733
Osterbrock D. E., Shuder J. M., 1982, ApJS, 49, 149
Pancoast A., Brewer B. J., Treu T., Park D., Barth A. J., Bentz M. C., Woo J-H., 2014, MNRAS, 445, 3073
Parker M. L. et al., 2014, MNRAS, 443, 1723
Patrick A. R., Reeves J. N., Porquet D., Markowitz A. G., Braito V., Lobban A. P., 2012, MNRAS, 426, 2522
Petterson J. A., 1977a, ApJ, 214, 550
Petterson J. A., 1977b, ApJ, 216, 827
Petterson J. A., 1978, ApJ, 226, 253
Peterson B. M., 2006, in Alloin D., Johnson R., Lira P., eds, Lecture Notes in Physics Vol. 693, Physics of Active Galactic Nuclei at all Scales. Springer, Berlin, p. 77
Phinney E. S., 1989, NATO Advanced Science Institutes (ASI) Series C, 290, 457
Ponti G. et al., 2010, MNRAS, 406, 2591
Porcas R., 1983, Nat, 302, 753
Pounds K., Reeves J., O'Brien P., Page K., Turner M., Nayakshin S., 2001, ApJ, 559, 181
Pounds K. A., Reeves J. N., Page K. L., O'Brien P. T., 2004, ApJ, 605, 670
Pringle J. E., 1996, MNRAS, 281, 357
Pringle J. E., Rees M. J., 1972, A&A, 21, 1
Puccetti S. et al., 2014, ApJ, 793, 26
Puccetti S. et al., 2016, A&A, 585, A157
Quillen A. C., 2001, ApJ, 563, 313
Raban D., Jaffe W., Röttgering H., Meisenheimer K., Tristram K. R. W., 2009, MNRAS, 394, 1325
Rachen J. P., Mannheim K., Biermann P. L., 1996, A&A, 310, 371
Rawlings S., Saunders R., 1991, Nat, 349, 138
Rees M. J., 1966, Nat, 211, 468
Reeves J. N., O'Brien P. T., Ward M. J., 2003, ApJ, 593, L65
Reeves J. N. et al., 2006, Astron. Nachr., 327, 1079
Risaliti G., Maiolino R., Salvati M., 1999, ApJ, 522, 157
Risaliti G., Elvis M., Nicastro F., 2002, ApJ, 571, 234
Risaliti G., Elvis M., Fabbiano G., Baldi A., Zezas A., 2005, ApJ, 623, L93
Risaliti G., Salvati M., Marconi A., 2011, MNRAS, 411, 2223
Risaliti G. et al., 2013, Nat, 494, 449
Rivers E. et al., 2015, ApJ, 815, 55
Rose M., Elvis M., Crenshaw M., Glidden A., 2015, MNRAS, 451, L11
Różańska A., Czerny B., Siemiginowska A., Dumont A.-M., Kawaguchi T., 2004, ApJ, 600, 96
Ruschel-Dutra D., Pastoriza M., Riffel R., Sales D. A., Winge C., 2014, MNRAS, 438, 3434
Saez C., Brandt W. N., Gallagher S. C., Bauer F. E., Garmire G. P., 2012, ApJ, 759, 42
Sako M. et al., 2001, A&A, 365, L168
Sales D. A., Pastoriza M. G., Riffel R., Winge C., Rodríguez-Ardila A., Carciofi A. C., 2011, ApJ, 738, 109
Salvaterra R. et al., 2009, Nat, 461, 1258
Sani E., Lutz D., Risaliti G., Netzer H., Gallo L. C., Trakhtenbrot B., Sturm E., Boller T., 2010, MNRAS, 403, 1246
Sazonov S., Churazov E., Krivonos R., 2015, MNRAS, 454, 1202
Schartel N. et al., 1996, MNRAS, 283, 1015
Schmid H. M., Appenzeller I., Camenzind M., Dietrich M., Heidt J., Schild H., Wagner S., 2001, A&A, 372, 59
Schmid H. M., Appenzeller I., Burch U., 2003, A&A, 404, 505
Schmidt G. D., Miller J. S., 1985, ApJ, 290, 517
Schmitt H. R., Kinney A. L., Storchi-Bergmann T., Antonucci R., 1997, ApJ, 477, 623
Schnittman J. D., Krolik J. H., 2010, ApJ, 712, 908
Schulz H., Komossa S., Schmitz C., Mücke A., 1999, A&A, 346, 764
Schweitzer M. et al., 2006, ApJ, 649, 79
Shakura N. I., Sunyaev R. A., 1973, A&A, 24, 337
Shang Z., Wills B. J., Wills D., Brotherton M. S., 2007, AJ, 134, 294
Shapovalova A. I. et al., 2004, A&A, 422, 925
Shen Y., Ho L. C., 2014, Nat, 513, 210
Shen S., Shao Z., Gu M., 2010, ApJ, 725, L210
Shu X. W., Wang J. X., Jiang P., Fan L. L., Wang T. G., 2007, ApJ, 657, 167
Simcoe R., McLeod K. K., Schachter J., Elvis M., 1997, ApJ, 489, 615
Simpson C., 2005, MNRAS, 360, 565
Smith D. A., Georgantopoulos I., Warwick R. S., 2001, ApJ, 550, 635
Smith J. E., Young S., Robinson A., Corbett E. A., Giannuzzo M. E., Axon D. J., Hough J. H., 2002, MNRAS, 335, 773
Spearman C., 1904, Amer. J. Psychol., 15, 72
Storchi-Bergmann T., Eracleous M., Ruiz M. T., Livio M., Wilson A. S., Filippenko A. V., 1997, ApJ, 489, 87
Storchi-Bergmann T., Winge C., Ward M. J., Wilson A. S., 1999, MNRAS, 304, 35
Sulentic J. W., 1989, ApJ, 343, 54
Tan Y., Wang J. X., Shu X. W., Zhou Y., 2012, ApJ, 747, L11
Teng S. H. et al., 2014, ApJ, 785, 19
Teng S. H. et al., 2015, ApJ, 814, 56
Tilton E. M., Shull J. M., 2013, ApJ, 774, 67
Tran H. D., 1995, ApJ, 440, 565
Tristram K. R. W., Burtscher L., Jaffe W., Meisenheimer K., Hönig S. F., Kishimoto M., Schartmann M., Weigelt G., 2014, A&A, 563, A82
Turner T. J. et al., 1999, ApJ, 510, 178
Urry C. M., Padovani P., 1995, PASP, 107, 803
Ursini F. et al., 2015, MNRAS, 452, 3266
Van Gorkom K. J., Wardle J. F. C., Rauch A. P., Gobeille D. B., 2015, MNRAS, 450, 4240
Vasudevan R. V., Fabian A. C., 2007, MNRAS, 381, 1235
Vasudevan R. V., Brandt W. N., Mushotzky R. F., Winter L. M., Baumgartner W. H., Shimizu T. T., Schneider D. P., Nousek J., 2013, ApJ, 763, 111
Véron-Cetty M.-P., Véron P., Gonçalves A. C., 2001, A&A, 372, 730
Vestergaard M., 2002, ApJ, 571, 733
Wada K., 2012, ApJ, 758, 66
Wada K., Papadopoulos P. P., Spaans M., 2009, ApJ, 702, 63
Walter R., Courvoisier T. J.-L., 1992, A&A, 266, 57
Walter R., Fink H. H., 1993, A&A, 274, 105

Walton D. J., Nardini E., Fabian A. C., Gallo L. C., Reis R. C., 2013, MNRAS, 428, 2901
Walton D. J. et al., 2014, ApJ, 788, 76
Wandel A., Petterson B. M., Malkan M. A., 1999, ApJ, 526, 579
Wang T., Brinkmann W., Bergeron J., 1996, A&A, 309, 81
Wilkes B. J. et al., 2013, ApJ, 773, 15
Wilkins D. R., Fabian A. C., 2012, MNRAS, 424, 1284
Wilkins D. R., Kara E., Fabian A. C., Gallo L. C., 2014, MNRAS, 443, 2746
Wills B. J., Brotherton M. S., 1995, ApJ, 448, L81
Wills B. J., Browne I. W. A., 1986, ApJ, 302, 56
Wills B. J., Wills D., Evans N. J. II, Natta A., Thompson K. L., Breger M., Sitko M. L., 1992, ApJ, 400, 96
Winkler H., 1992, MNRAS, 257, 677
Winter L. M., Mushotzky R. F., Tueller J., Markwardt C., 2008, ApJ, 674, 686
Winter L. M., Mushotzky R. F., Reynolds C. S., Tueller J., 2009, ApJ, 690, 1322
Winter L. M., Lewis K. T., Koss M., Veilleux S., Keeney B., Mushotzky R. F., 2010, ApJ, 710, 503
Woo J-H., Urry C. M., 2002, ApJ, 579, 530
Woo J-H., Kim J-G., Park D., Bae H-J., Kim J-H., Lee S-E., Kim S. C., Kwon H-J., 2014, Journal of Korean Astronomical Society, 47, 167
Woo J-H., Yoon Y., Park S., Park D., Kim S. C., 2015, ApJ, 801, 38
Wu X-B., Han J. L., 2001, ApJ, 561, L59
Xiao T., Barth A. J., Greene J. E., Wills B. J., Bailey J. A., Ward M. J., Axon D. J., 2011, ApJ, 739, 28
Yang H., Wang J., Liu T., 2015, ApJ, 799, 91
Young S., 2000, MNRAS, 312, 567
Young S., Hough J. H., Efstathiou A., Wills B. J., Bailey J. A., Ward M. J., Axon D. J., 1996, MNRAS, 281, 1206
Zakamska N. L., Greene J. E., 2014, MNRAS, 442, 784
Zhang T-Z., Wu X-B., 2002, CJA&A, 2, 487
Zitrin A. et al., 2015, ApJ, 810, L12
Zoghbi A. et al., 2015, ApJ, 799, L24

APPENDIX A: DATA TABLES

Table A1. Archival data listing the 124 Seyfert galaxies with identified nuclear inclination measurements. The redshifts are obtained through SIMBAD. The central black-hole masses are in logarithmic units and taken from the AGN black hole data base (Bentz & Katz 2015), Kaspi et al. (2000), Vestergaard (2002), Vasudevan & Fabian (2007), Esquej et al. (2014) and Feng, Shen & Li (2014). The AGN classification types are also indicated for completeness. The different main methods (labelled as IR, X, NLR and VEL) used to determine the inclination of the system are presented in the text. References: Wil92, Wills et al. (1992); Nan97, Nandra et al. (1997); Sto97, Storchi-Bergmann et al. (1997); Car98, Carilli, Wrobel & Ulvestad (1998); Mar98, Marquez et al. (1998); Sto99, Storchi-Bergmann et al. (1999); Obr01, O'Brien et al. (2001); Sch01, Schmid et al. (2001); Smi01, Smith, Georgantopoulos & Warwick (2001); Wu01, Wu & Han (2001); Zha02, Zhang & Wu (2002); Sch03, Schmid et al. (2003); Bec04, Beckmann et al. (2004); Cho07, Chou et al. (2007); Fan07, Fan (2007); Hon07, Hönig et al. (2007); Min07, Miniutti et al. (2007); Nan07, Nandra et al. (2007); Hic08, Hicks & Malkan (2008); Mor09, Mor et al. (2009); Bor10, Borguet & Hutsemékers (2010); Nog10, Noguchi et al. (2010); Pon10, Ponti et al. (2010); Alo11, Alonso-Herrero et al. (2011); Bha11, Bhayani & Nandra (2011); Sal11, Sales et al. (2011); Dau12, Dauser et al. (2012); Tan12, Tan et al. (2012); Fis13, Fischer et al. (2013); Kaw13, Kawamuro et al. (2013); Ris13, Risaliti et al. (2013); Wal13, Walton et al. (2013); Agi14, Agís-González et al. (2014); Bal14, Baloković et al. (2014); Lah14, Laha et al. (2014); Mar14, Marinucci et al. (2014); Pan14, Pancoast et al. (2014); Rus14, Ruschel-Dutra et al. (2014); Riv15, Rivers et al. (2015).

Object	Type	Redshift	BH mass (log)	L_{bol} (log erg s^{-1})	Inclination (°)	Ref.	Method
0019+0107	BAL QSO	2.123	–	–	90.0	Bor10	OTHER
0145+0416	BAL QSO	2.03	–	–	80.0	Bor10	OTHER
0226–1024	BAL QSO	2.256	–	–	87.0	Bor10	OTHER
0842+3431	BAL QSO	2.13	–	–	78.0	Bor10	OTHER
1235+1453	BAL QSO	2.686	–	–	76.0	Bor10	OTHER
1333+2840	BAL QSO	1.91	–	–	80.0	Bor10	OTHER
1413+1143	BAL QSO	2.560	–	–	88.0	Bor10	OTHER
1H0419–577	1.5	0.104000	8.30	46.38	51.0^{+4}_{6}	Wal13	X
1H0707–495	NLS1	0.040568	6.85	44.48	$48.8^{+1.3}_{-1.2}$	Dau12	X
3C 120	1.5	0.033573	7.74	45.34	$22.0^{+9.3}_{-7.7}$	Wu01	BH–σ
4C 13.41	1.0	0.24064	–	46.3	35.0	Mor09	IR
Akn 120	BLS1	0.0323	8.07	44.91	42.0	Zha02	BH–σ
Akn 564	NLS1	0.024917	6.41	44.77	26.0	Zha02	BH–σ
Arp 151	BLS1	0.021091	6.62	43.7	$25.2^{+3.3}_{-3.4}$	Pan14	OTHER
Circinus	2.0	0.001449	6.42	43.59	65.0	Fis13	NLR
ESO 323–G077	NLS1	0.014904	7.40	43.9	45.0	Sch03	OTHER
ESO 362–G18	1.5	0.012445	7.65	44.11	53.0 ± 5	Agi14	OTHER
ESO 511–G30	1.0	0.022389	8.40	44.41	59 ± 10	Lah14	OTHER
Fairall 51	1.5	0.014361	8.00	43.95	45.0	Sch01	OTHER
Fairall 9	BLS1	0.048175	8.20	45.23	35.0	Zha02	BH–σ
I Zw 1	NLS1	0.060875	7.24	44.98	8.0	Mor09	IR
IC 2560	2.0	0.009757	6.48	42.7	66.0^{+7}_{-4}	Bal14	X
IC 4329A	BLS1	0.01613	6.77	44.78	$10.0^{+13.0}_{-10.0}$	Nan97	X
IC 5063	2.0	0.011274	7.74	44.53	82.0^{+5}_{-9}	Alo11	IR
IRAS 00521–7054	2.0	0.068900	–	49.43	$37^{+4/+13}_{-4/-7}$	Tan12	X
IRAS 13224–3809	1.0	0.0658	7.00	44.95	52.0	Pon10	X
IRAS 13349+2438	2.0	0.10853	8.75	46.3	52.0	Wil92	OTHER
K 348–7	1.0	0.2341	8.58	46.16	35.0	Mor09	IR
MCG–2–8–39	2.0	0.029894	7.85	42.57	60.0	Nog10	X
MCG–3–34–64	1.5	0.017092	7.69	44.8	27.0 ± 17	Min07	X

Table A1 – *continued*

Object	Type	Redshift	BH mass (log)	$L_{\rm bol}$ (log erg s^{-1})	Inclination (°)	Ref.	Method
MCG–3–58–7	2.0	0.031462	–	44.7	60.0	Nog10	X
MCG–6–30–15	1.5	0.00758	6.46	43.85	$34.0^{+5.0}_{-6.0}$	Nan97	X
MCG+8–11–11	1.5	0.02004	8.08	44.43	45.0	Bha11	X
Mrk 1014	1.0	0.16274	8.03	46.26	16.0	Mor09	IR
Mrk 1018	1.0	0.042436	8.6	44.9	$45^{+14}_{-10/-15}$	Wal13	X
Mrk 1066	2.0	0.012082	7.01	44.55	80.0	Fis13	NLR
Mrk 110	1.5	0.03552	7.29	44.71	$37.4^{+9.2}_{-9.5}$	Wu01	BH–σ
Mrk 1239	NLS1	0.0196	6.38	44.65	7.0	Zha02	BH–σ
Mrk 1298	BLS1	0.06	5.00	45.54	28.0	Mor09	IR
Mrk 1310	1.0	0.019560	8.10	43.5	$6.6^{+5.0}_{-2.5}$	Pan14	OTHER
Mrk 1383	BLS1	0.087	8.92	45.78	30.0	Mor09	IR
Mrk 176	2.0	0.02646	8.00	45.84	60.0	Nog10	X
Mrk 231	BLS1	0.04147	7.94	46.18	45.0	Car98	OTHER
Mrk 273	2.0	0.03734	8.22	47	60.0	Nog10	X
Mrk 279	BLS1	0.030601	7.43	44.36	35.0	Fis13	NLR
Mrk 3	2.0	0.013443	8.26	44.54	85.0	Fis13	NLR
Mrk 304	BLS1	0.066293	–	44.56	40.0	Mor09	IR
Mrk 335	NLS1	0.025418	7.23	44.69	20.0	Zha02	BH–σ
Mrk 34	2.0	0.05095	7.80	44.78	65.0	Fis13	NLR
Mrk 348	2.0	0.015034	7.21	44.27	60.0	Smi01	X
Mrk 359	NLS1	0.01684	6.23	43.55	30.0	Obr01	X
Mrk 463	2.0	0.050382	7.88	45.28	60.0	Nog10	X
Mrk 478	NLS1	0.079	7.33	45.56	25.0	Zha02	BH–σ
Mrk 486	BLS1	0.039	7.03	45.04	16.0	Zha02	BH–σ
Mrk 50	1.0	0.023433	7.57	44.34	9^{+7}_{-5}	Pan14	OTHER
Mrk 509	BLS1	0.03501	8.05	45.03	19.0	Zha02	BH–σ
Mrk 573	2.0	0.017285	7.58	44.44	60.0	Fis13	NLR
Mrk 590	BLS1	0.02609	7.57	44.63	$17.8^{+6.1}_{-5.9}$	Wu01	BH–σ
Mrk 6	1.5	0.018676	8.10	44.56	26.0	Bha11	X
Mrk 705	NLS1	0.0288	6.92	44.74	16.0	Zha02	BH–σ
Mrk 707	NLS1	0.05026	6.63	44.79	15.0	Zha02	BH–σ
Mrk 766	NLS1	0.01271	6.63	44.23	$36.0^{+8.0}_{-7.0}$	Nan97	X
Mrk 78	2.0	0.03715	8.14	44.59	60.0	Fis13	NLR
Mrk 79	BLS1	0.022185	7.61	44.57	58.0	Zha02	BH–σ
Mrk 817	1.5	0.031455	7.60	44.99	$41.6^{+8.5}_{-7.5}$	Wu01	BH–σ
Mrk 841	1.5	0.03642	7.90	45.84	$26.0^{+8.0}_{-5.0}$	Nan97	X
Mrk 876	BLS1	0.138512	8.95	45.81	27.0	Mor09	IR
Mrk 877	BLS1	0.112	8.44	45.33	20.0	Mor09	IR
Mrk 896	NLS1	0.026784	6.58	43.89	15.0	Zha02	BH–σ
NGC 1068	2.0	0.00381	7.59	44.3	70.0	Hon07	IR
NGC 1097	LINER	0.004218	8.15	47.59	34.0	Sto97	OTHER
NGC 1320	2.0	0.0092	7.18	43.86	68.0^{+3}_{-2}	Bal14	X
NGC 1365	1.8	0.005476	8.20	43.1	57.5 ± 2.5	Ris13	X
NGC 1386	1.9/2.0	0.002905	7.42	43.38	81.0^{+6}_{-8}	Rus14	IR
NGC 1566	1.5	0.005036	6.92	44.45	30.0	Kaw13	X
NGC 1667	2.0	0.015204	7.62	44.69	72.0	Fis13	NLR
NGC 2110	1.9/2.0	0.007579	8.30	43.7	53.0	Sto99	OTHER
NGC 2655	LINER	0.004670	8.50	42.08	60.0	Nog10	X
NGC 2992	2.0	0.007296	7.72	43.92	70.0	Mar98	OTHER
NGC 3227	1.5	0.00365	6.77	43.86	14.2 ± 2.5	Hic08	NLR
NGC 3281	2.0	0.010674	8.60	43.8	69^{+11}_{-11}	Sal11	IR
NGC 3516	1.5	0.008816	7.39	44.29	26.0^{+3}_{-4}	Nan97	X
NGC 3783	1.5	0.009755	7.37	44.41	15.0	Fis13	NLR
NGC 4051	NLS1	0.00216	6.13	43.56	$19.6^{+10.4}_{-6.6}$	Wu01	BH–σ
NGC 4151	1.5	0.003262	7.56	43.73	9.0^{+18}_{-9}	Nan97	X
NGC 424	2.0	0.01184	7.78	44.85	69.0^{+5}_{-4}	Bal14	X
NGC 4388	2.0	0.00862	7.23	44.1	60.0 – 63	Bec04	OTHER
NGC 4395	1.8	0.00106	5.45	41.37	15.0^{+12}_{-15}	Nan07	X
NGC 4507	1.9/2.0	0.011907	7.65	44.4	47.0	Fis13	NLR
NGC 4593	BLS1	0.008344	6.88	44.09	21.6 ± 10.5	Wu01	BH–σ
NGC 4941	2.0	0.00369	6.90	43.0	70.0	Kaw13	X
NGC 4945	2.0	0.001878	6.15	43.4	62.0	Cho07	OTHER

Table A1 – *continued*

Object	Type	Redshift	BH mass (log)	L_{bol} (log erg s^{-1})	Inclination (°)	Ref.	Method
NGC 5506	NLS1	0.00589	7.95	44.3	80.0	Fis13	NLR
NGC 5548	1.5	0.01627	7.72	44.83	$47.3^{+7.6}_{-6.9}$	Wu01	BH–σ
NGC 5643	2.0	0.00399	7.40	42.3	65.0	Fis13	NLR
NGC 6240	2.0	0.024480	8.94	44.3	63.3	Fan07	OTHER
NGC 7172	2.0	0.008616	7.67	43.3	77.0^{+8}_{-14}	Alo11	IR
NGC 7213	LINER	0.005869	7.74	44.3	$21.0^{+9.0}_{-12.0}$	Rus14	IR
NGC 7314	1.9	0.004771	6.70	43.23	42.0^{+3}_{-4}	Nan07	X
NGC 7469	1.5	0.01588	6.96	45.28	15.0 ± 1.8	Hic08	NLR
NGC 7582	2.0	0.00525	7.74	43.3	65.0	Riv15	X
NGC 7674	2.0	0.02998	7.56	45.47	60.0	Fis13	NLR
PDS 456	1.0	0.184000	9.00	47.00	70^{+3}_{-5}	Wal13	X
PG 0026+129	NLS1	0.142	8.49	45.39	43.0	Mor09	IR
PG 1001+054	NLS1	0.16012	7.65	45.76	38.0	Mor09	IR
PG 1211+143	NLS1	0.0809	7.37	45.81	31.0	Zha02	BH–σ
PG 1244+026	NLS1	0.04813	6.11	44.13	31.0	Mor09	IR
PG 1302–102	1.0	0.2784	8.94	46.33	32.0	Mor09	IR
PG 1411+442	BLS1	0.09	8.54	45.58	14.0	Mor09	IR
PG 1435–067	BLS1	0.126	8.24	45.5	38.0	Mor09	IR
PG 1448+273	NLS1	0.06451	6.92	45.02	53.0	Mor09	IR
PG 1626+554	BLS1	0.133	8.37	45.85	31.0	Mor09	IR
PG 1700+518	NLS1	0.292	8.79	46.56	43.0	Mor09	IR
PG 2251+113	1.0	0.325252	8.96	46.56	67.0	Mor09	IR
RBS 1124	BLS1	0.208000	8.26	45.53	66^{+5}_{-12}	Wal13	X
SBS 1116+583A	1.0	0.027872	6.99	–	$18.2^{+8.4}_{-5.9}$	Pan14	OTHER
Swift J2127.4+5654	NLS1	0.014400	7.18	44.54	49.0 ± 2.0	Mar14	X
TON 1388	1.0	0.1765	8.50	45.92	39.0	Mor09	IR
TON 1542	BLS1	0.06355	7.93	45.27	28.0	Mor09	IR
TON 1565	1.0	0.18291	8.21	45.89	37.0	Mor09	IR
Ton S180	NLS1	0.061980	7.30	45.70	$60^{+3/+10}_{-1/-10}$	Wal13	X
UGC 3973	1.5	0.022189	8.10	44.31	19.0 ± 6	Lah14	OTHER
UGC 6728	1.0	0.006518	6.30	43.0	<55	Wal13	X
VII Zw 244	BLS1	0.131344	–	45.35	23.0	Mor09	IR

Table A2. Inclinations of 19 Seyfert nuclei derived from the black-hole mass–bulge velocity dispersion relation. Note that the data taken from Zhang & Wu (2002) are restricted to AGNs with measured BLR size and FWHM of Hβ emission line. All AGNs are type 1 AGNs. References: Wu01, Wu & Han (2001); Zha02, Zhang & Wu (2002).

Object	Inclination (°)	Reference
3C 120	$22.0^{+9.3}_{-7.7}$	Wu01
Akn 120	42.0	Zha02
Fairall 9	35.0	Zha02
IC 4329A	5.0	Zha02
Mrk 110	$37.4^{+9.2}_{-9.5}$	Wu01
Mrk 279	13.0	Zha02
Mrk 335	20.0	Zha02
Mrk 509	19.0	Zha02
Mrk 590	$17.8^{+6.1}_{-5.9}$	Wu01
Mrk 79	$58.5^{+21.7}_{-27.9}$	Wu01
Mrk 817	$41.6^{+8.5}_{-7.5}$	Wu01
NGC 3227	$37.5^{+17.3}_{-25.4}$	Wu01
NGC 3516	38.3 ± 7.6	Wu01
NGC 3783	38.0	Zha02
NGC 4051	$19.6^{+10.4}_{-6.6}$	Wu01
NGC 4151	$60.0^{+30.0}_{-30.6}$	Wu01
NGC 4593	21.6 ± 10.5	Wu01
NGC 5548	$43.7^{+7.6}_{-6.9}$	Wu01
NGC 7469	13.0	Zha02

Table A3. Inclinations of 54 Seyfert nuclei, as determined by fitting their X-ray spectra with disc reflection models in special and general relativistic environments. See also Middleton et al. (2016) and references therein. References: Nan97, Nandra et al. (1997); Smi01, Smith et al. (2001); Min07, Miniutti et al. (2007); Nan07, Nandra et al. (2007); Nog10, Noguchi et al. (2010); Bha11, Bhayani & Nandra (2011); Gal11, Gallo et al. (2011); Dau12, Dauser et al. (2012); Loh12, Lohfink et al. (2012); Pat12, Patrick et al. (2012); Tan12, Tan et al. (2012); Kaw13, Kawamuro et al. (2013); Loh13, Lohfink et al. (2013); Wal13, Walton et al. (2013); Agi14, Agís-González et al. (2014); Bal14, Baloković et al. (2014); Mar14, Marinucci et al. (2014); Par14, Parker et al. (2014); Wal14, Walton et al. (2014); Chi15, Chiang et al. (2015); Riv15, Rivers et al. (2015); Zog15, Zoghbi et al. (2015).

Object	Inclination (°)	Reference
1H 0419–577	51.0^{+4}_{-6}	Wal13
1H 0707–495	$52.0^{+1.7}_{-1.8}$	Dau12
3C 120	5^{+4}_{-5}	Loh13
Akn 120	54.0^{+6}_{-5}	Wal13
Akn 564	$64.0^{+1/+6}_{-11}$	Wal13
ESO 362–G18	53.0 ± 5	Agi14
Fairall 9	48.0^{+6}_{-2}	Loh12
IC 2560	66.0^{+7}_{-4}	Bal14
IC 4329A	10.0^{+13}_{-10}	Nan97
IRAS 00521–7054	$37.0^{+4/+13}_{-4/-7}$	Tan12
IRAS 13224–3809	$65.0^{+1/+5}_{-1}$	Chi15

Table A3 – *continued*

Object	Inclination (°)	Reference
MCG–2–8–39	60.0	Nog10
MCG–3–34–64	27.0 ± 17	Min07
MCG–3–58–7	60.0	Nog10
MCG–6–30–15	$34.0^{+5.0}_{-6.0}$	Nan97
MCG+8–11–11	45.0^{+40}_{-8}	Bha11
Mrk 1018	$45.0^{+14}_{-10/-15}$	Wal13
Mrk 110	36.0^{+19}_{-12}	Bha11
Mrk 176	60.0	Nog10
Mrk 273	60.0	Nog10
Mrk 335	65.0 ± 1	Par14
Mrk 348	60.0	Smi01
Mrk 359	47.0 ± 6	Wal13
Mrk 463	60.0	Nog10
Mrk 509	<18	Wal13
Mrk 590	47.0^{+38}_{-47}	Bha11
Mrk 6	26.0^{+59}_{-7}	Bha11
Mrk 766	36.0^{+8}_{-7}	Nan97
Mrk 79	24.0 ± 1	Gal11
Mrk 841	45.0^{+7}_{-5}	Wal13
NGC 1320	68.0^{+3}_{-2}	Bal14
NGC 1365	63 ± 4	Wal14
NGC 1566	30.0	Kaw13
NGC 2110	0.0^{+51}_{-0}	Bha11
NGC 2655	60.0	Nog10
NGC 3227	47.0^{+3}_{-2}	Pat12
NGC 3516	33.0^{+3}_{-9}	Nan07
NGC 3783	3.0^{+18}_{-3}	Nan07
NGC 4051	25.0^{+12}_{-4}	Nan97
NGC 4151	33.0^{+1}_{-3}	Nan07
NGC 424	69.0^{+5}_{-4}	Bal14
NGC 4593	24.0^{+28}_{-15}	Nan07
NGC 4941	70.0	Kaw13
NGC 5506	46.0^{+4}_{-4}	Bha11
NGC 5548	3.0^{+82}_{-3}	Bha11
NGC 7213	0.0^{+64}_{-0}	Bha11
NGC 7469	<54	Wal13
NGC 7582	65.0	Riv15
PDS 456	70^{+3}_{-5}	Wal13
PG 1211+143	$28.0^{+7/+22}_{-7}$	Zog15
RBS 1124	66^{+5}_{-12}	Wal13
Swift J2127.4+5654	49.0 ± 2.0	Mar14
Ton S180	$60^{+3/+10}_{-1/-10}$	Wal13
UGC 6728	<55	Wal13

Table A4. Inclinations of 37 Seyfert nuclei, as determined by fitting their IR spectra with radiative transfer in clumpy environments; see Section 2. References: Hon07, Hönig et al. (2007); Mor09, Mor et al. (2009); Alo11, Alonso-Herrero et al. (2011); Sal11, Sales et al. (2011); Rus14, Ruschel-Dutra et al. (2014).

Object	Inclination (°)	Reference
Circinus	66.0^{+7}_{-4}	Alo11
I Zw 1	8	Mor09
IC 4329A	51.0^{+8}_{-8}	Alo11
IC 5063	82.0^{+5}_{-9}	Alo11
K 348–7	35	Mor09
Mrk 304	40	Mor09
Mrk 478	26	Mor09
Mrk 876	27	Mor09
Mrk 877	20	Mor09

Table A4 – *continued*

Object	Inclination (°)	Reference
Mrk 1014	16	Mor09
Mrk 1298	28	Mor09
Mrk 1383	30	Mor09
NGC 1068	70	Hon07
NGC 1386	81.0^{+6}_{-8}	Rus14
NGC 2110	43.0^{+8}_{-8}	Alo11
NGC 3227	24.0^{+11}_{-15}	Alo11
NGC 3281	69.0^{+11}_{-11}	Sal11
NGC 4151	63.0^{+4}_{-7}	Alo11
NGC 5506	34.0^{+6}_{-6}	Alo11
NGC 7172	77.0^{+8}_{-14}	Alo11
NGC 7213	21.0^{+9}_{-12}	Rus14
NGC 7469	58.0^{+3}_{-4}	Alo11
NGC 7674	63.0^{+9}_{-10}	Alo11
PG 0026+129	43	Mor09
PG 1001+054	38	Mor09
PG 1244+026	31	Mor09
PG 1302–102	32	Mor09
PG 1411+442	14	Mor09
PG 1435–067	38	Mor09
PG 1448+273	53	Mor09
PG 1626+554	31	Mor09
PG 1700+518	43	Mor09
PG 2251+113	67	Mor09
TON 1388	39	Mor09
TON 1542	28	Mor09
TON 1565	37	Mor09
VII Zw 244	23	Mor09

Table A5. Inclinations of 17 Seyfert nuclei, as determined by their NLR kinematics. A standard $\pm 5^\circ$ uncertainty is added to the inclinations by the authors (e.g. Rose et al. 2015). Reference: Fis13, Fischer et al. (2013).

Object	Inclination (°)	Reference
Circinus	65	Fis13
Mrk 3	85	Fis13
Mrk 34	65	Fis13
Mrk 78	60	Fis13
Mrk 279	35	Fis13
Mrk 573	60	Fis13
Mrk 1066	80	Fis13
NGC 1068	85	Fis13
NGC 1667	72	Fis13
NGC 3227	15	Fis13
NGC 3783	15	Fis13
NGC 4051	12	Fis13
NGC 4151	45	Fis13
NGC 4507	47	Fis13
NGC 5506	80	Fis13
NGC 5643	65	Fis13
NGC 7674	60	Fis13

Table A6. Archival X-ray column density for 104/124 Seyfert galaxies. The hydrogen column density is ionized for type 1s and cold for type 2s. References: Wal92, Walter & Courvoisier (1992); Wal93, Walter & Fink (1993); Bol96, Boller, Brandt & Fink (1996); Kar97, Kartje et al. (1997); Rac96, Rachen, Mannheim & Biermann (1996); Sch96, Schartel et al. (1996); Wan96, Wang, Brinkmann & Bergeron (1996); Ris99, Risaliti, Maiolino & Salvati (1999); Sak01, Sako et al. (2001); Ris02, Risaliti, Elvis & Nicastro (2002); Gua04, Guainazzi et al. (2004); Mat04a, Matt et al. (2004a); Pou04, Pounds et al. (2004); Roz04, Różańska et al. (2004); Bia05a, Bianchi et al. (2005a); Bia05b, Bianchi et al. (2005b); Shu07, Shu et al. (2007); Jim08a, Jiménez-Bailón et al. (2008a); Jim08b, Jiménez-Bailón et al. (2008b); Mar08, González Martín (2008); Win08, Winter et al. (2008); Mar09, Markowitz et al. (2009); Win09, Winter et al. (2009); Era10, Eracleous, Hwang & Flohic (2010); Gal11, Gallo et al. (2011); Gil10, Gilli et al. (2010); Min10, Miniutti et al. (2010); Win10 , Winter et al. (2010); Cre12, Crenshaw & Kraemer (2012); Ich12, Ichikawa et al. (2012); Sae12, Saez et al. (2012); Tan12, Tan et al. (2012); Vas13, Vasudevan et al. (2013); Lir13, Lira et al. (2013); Are14, Arévalo et al. (2014); Bal14, Baloković et al. (2014); Bau15, Bauer et al. (2015); Gan14, Gandhi et al. (2014); Mar14, Marinucci et al. (2014); Puc14, Puccetti et al. (2014); Rus14, Ruschel-Dutra et al. (2014); Ten14, Teng et al. (2014); Meh15, Mehdipour et al. (2015); Nar15, Nardini et al. (2015); Puc16, Puccetti et al. (2016); Ten15, Teng et al. (2015); Urs15, Ursini et al. (2015).

Object	$n_{\rm H}$ ($\times 10^{22}$ cm^{-2})	Reference
1H0419–577	4.3 ± 0.4	Pou04
3C 120	0.16	Win09
Akn 120	0.02	Win09
Akn 564	0.073 ± 0.004	Bol96
Arp 151	$0.2173^{+0.0059}_{-0.0199}$	Win09
Circinus	600 – 1000	Are14
ESO 323–G077	$5.85^{+0.12}_{-0.11}$	Jim08a
ESO 362–G18	26.6	Win09
ESO 511–G30	0.098	Win09
Fairall 51	1.6 ± 0.2	Jim08b
Fairall 9	0.023	Win09
I Zw 1	0.065 ± 0.007	Bol96
IC 2560	>1000	Bal14
IC 4329A	0.61	Win09
IC 5063	25	Win09
IRAS 00521–7054	7.0 ± 0.8	Tan12
IRAS 13349+2438	2.5 ± 1.5	Sak01
MCG–2–8–39	31.6	Lir13
MCG–3–34–64	40.7	Win09
MCG–3–58–7	25.1	Lir13
MCG–6–30–15	0.19	Win09
MCG+8–11–11	0.25	Win09
Mrk 1018	0.01 ± 0.016	Wal93
Mrk 1066	>100	Ris99
Mrk 110	1.78	Win09
Mrk 1239	0.083 ± 0.016	Bol96
Mrk 1310	$0.242^{+0.0024}_{-0.0018}$	Win09
Mrk 1383	0.021 ± 0.011	Wal93
Mrk 231	12 ± 1	Ten14
Mrk 273	$43.8^{+9.5}_{-5.7}$	Ten15
Mrk 279	0.013	Win09
Mrk 3	136^{+3}_{-4}	Bia05a
Mrk 304	0.0145	Kar97
Mrk 335	$0.03^{+0.05}_{-0.03}$	Wal92
Mrk 34	250 – 1000	Gan14
Mrk 348	16	Win09
Mrk 359	0.05 ± 0.007	Bol96
Mrk 463	0.2382 ± 0.0003	Vas13
Mrk 478	0.02 ± 0.003	Bol96
Mrk 50	0.006	Win09
Mrk 509	0.015	Win09

Table A6 – *continued*

Object	$n_{\rm H}$ ($\times 10^{22}$ cm^{-2})	Reference
Mrk 573	>100	Shu07
Mrk 590	0.027	Win09
Mrk 6	3.26	Win09
Mrk 705	0.039 ± 0.013	Wal93
Mrk 766	0.525	Win09
Mrk 78	57.5 ± 5.8	Gil10
Mrk 79	<0.0063	Ich12
Mrk 817	0.1285 ± 0.0008	Win10
Mrk 841	0.219	Win09
Mrk 876	$0.043^{+0.009}_{-0.008}$	Sch96
Mrk 877	$0.008^{+0.033}_{-0.008}$	Sch96
Mrk 896	0.034 ± 0.004	Bol96
NGC 1068	15 – 1000	Bau14
NGC 1097	0.023	Era10
NGC 1320	400^{+20}_{-10}	Bal14
NGC 1365	450	Win09
NGC 1386	140^{+10}_{-20}	Rus14
NGC 1566	0.007 ± 0.011	Wal93
NGC 1667	>100	Bia05b
NGC 2110	2.84	Win09
NGC 2655	$30.2^{+39.47}_{-24.21}$	Gon08
NGC 2992	1.19	Win09
NGC 3227	0.35 ± 0.18	Mar09
NGC 3281	86.3	Win09
NGC 3516	0.353	Win09
NGC 3783	3.6 ± 0.5	Cre12
NGC 4051	2.1 ± 1.1	Cre12
NGC 4151	9.4 ± 2.8	Cre12
NGC 424	300 ± 10	Bal14
NGC 4388	36.2	Win09
NGC 4395	3.3	Win09
NGC 4507	43.9 ± 5.7	Mat04a
NGC 4593	0.031	Win09
NGC 4941	$0.2412^{+0.0012}_{-0.0017}$	Vas13
NGC 4945	355	Puc14
NGC 5506	3.7 ± 0.8	Ris02
NGC 5548	1.2 – 9.6	Meh15
NGC 5643	70.7^{+30}_{-10}	Gua04
NGC 6240	150	Puc16
NGC 7172	8.19	Win09
NGC 7213	50^{+20}_{-16}	Urs15
NGC 7314	1.16	Win09
NGC 7469	0.041	Win09
NGC 7582	300	Riv15
NGC 7674	> 1000	Bia05b
PDS 456	12.1 ± 1	Nar15
PG 0026+129	0.0522 ± 0.0105	Rac96
PG 1001+054	0.0233	Wan96
PG 1211+143	0.03 ± 0.01	Wal93
PG 1244+026	0.0311 ± 0.0049	Wan96
PG 1302–102	0.027 ± 0.0076	Rac96
PG 1411+442	0.0118 ± 0.0094	Rac96
PG 1448+273	0.044 ± 0.016	Wal93
PG 1626+554	$0.03^{+0.019}_{-0.013}$	Sch96
PG 1700+518	<0.12	Sae12
RBS 1124	6.0^{+3}_{-2}	Min10
Swift J2127.4+5654	0.213 ± 0.005	Mar14
TON 1542	0.037 ± 0.019	Wal93
Ton S180	$0.037^{+0.023}_{-0.022}$	Roz04
UGC 3973	0.734 ± 0.019	Wal93
UGC 6728	$0.01^{+0.02}_{-0.01}$	Win08
VII Zw 244	$0.061^{+0.13}_{-0.044}$	Sch96

Table A7. Archival optical FWHM measurements of the Hβ λ4861 line for 74/90 type 1 AGNs. Some objects show large, double-peaked, Balmer line profiles and are identified with the superscript [a]. A larger fraction of AGNs, which need to be identified, might show similar characteristics. References: Ost82, Osterbrock & Shuder (1982); Mac84, MacKenty & Stockton (1984); Bro87, Browne & Murphy (1987); Goo89, Goodrich (1989); Sul89, Sulentic (1989); Mar92, Marziani et al. (1992); Win92, Winkler (1992); Esp94, Espey et al. (1994); Bol96, Boller et al. (1996); You96, Young et al. (1996); Bra97, Brandt, Mathur & Elvis (1997); Kol97, Kollatschny & Dietrich (1997); Gru99, Grupe et al. (1999); Sch99, Schulz et al. (1999); Tur98, Turner et al. (1999); Ver01, Véron-Cetty, Véron & Gonçalves (2001); Ree03, Reeves, O'Brien & Ward (2003); Sch03, Schmid et al. (2003); Ben06, Bennert et al. (2006a); Kol06, Kollatschny, Zetzl & Dietrich (2006); Sha07, Shang et al. (2007); Mal08, Malizia et al. (2008); Win09, Winter et al. (2009); Min10, Miniutti et al. (2010); San10, Sani et al. (2010); Edr12, Edri et al. (2012); Til13, Tilton & Shull (2013); Agi14, Agís-González et al. (2014); Fen14, Feng, Shen & Li (2014); Mur14, La Mura et al. (2014); Don15, Done & Jin (2016); Gra15, Graham et al. (2015).

Object	FWHM Hβ (km s^{-1})	Reference
1H0419–577	4200 ± 250	
1H0707–495	940	Don15
3C 120	2419 ± 29	Fen14
4C 13.41	6800	Bro87
Akn 120[a]	5987 ± 54	Fen14
Akn 564	865	Ver01
Arp 151	3407 ± 35	Fen14
ESO 323–G077	2100	Sch03
ESO 362–G18	5240 ± 500	Agi14
ESO 511–G30	2500	Win92
Fairall 51	3330 ± 300	Ben06
Fairall 9	5618 ± 107	Fen14
I Zw 1	1240	Bol96
IC 4329A[a]	6000	Mar92
IRAS 00521+7054	817	You96
IRAS 13224–3809	650	Bra97
K 348–7	3225	Til13
MCG–3–34–64	–	–
MCG–6–30–15	1990 ± 200	
MCG+8–11–11	3630	Ost82
Mrk 6	4512 ± 38	Fen14
Mrk 6	4512 ± 38	Fen14
Mrk 50	4621 ± 30	Fen14
Mrk 79	4735 ± 44	Kol06
Mrk 110	2194 ± 64	Fen14
Mrk 231	3000	Ver01
Mrk 279	5208 ± 95	Fen14
Mrk 304	4600	Sul89
Mrk 335	2182 ± 53	Fen14
Mrk 359	900	Ver01
Mrk 478	1270	Ver01
Mrk 486	1680	Ver01
Mrk 509	3595 ± 24	Fen14
Mrk 590	2966 ± 56	Fen14
Mrk 705	1790	Ver01
Mrk 707	1295	Ver01
Mrk 766	1630	Ver01
Mrk 817	4937 ± 120	Fen14
Mrk 841	5300	Bra97
Mrk 876	5017	Sul89
Mrk 877	3790	Sul89
Mrk 896	1135	Ver01
Mrk 1014	2308	Mac84
Mrk 1018	6940 ± 760	Mur14
Mrk 1239	1075	Ver01
Mrk 1298	2200	Goo89
Mrk 1310	2731 ± 51	Fen14
Mrk 1383	5420	Sul89
NGC 1097[a]	–	–
NGC 1365	3586	Sch99
NGC 1566	1800	Win92
NGC 3227	4494 ± 19	Fen14
NGC 3516	5527 ± 17	Fen14
NGC 3783	3634 ± 41	Fen14
NGC 4051	1565 ± 80	Fen14
NGC 4151	6794 ± 161	Fen14
NGC 4395	1175 ± 325	Edr12
NGC 4593	3900	Kol97
NGC 5548[a]	12404 ± 20	Fen14
NGC 7213	3200	Win92
NGC 7314	–	–
NGC 7469	3296 ± 75	Fen14
PDS 456	3000	Ree03
PG 0026+129	2598 ± 57	Fen14
PG 1001+054	1125 ± 30	Sha07
PG 1211+143	1975	Ver01
PG 1244+026	740	Ver01
PG 1302–102	4450 ± 150	Gra15
PG 1411+442	2392 ± 56	Fen14
PG 1435–067	3180	San10
PG 1448+273	820	Bol96
PG 1626+554	4618	Til13
PG 1700+518	2230 ± 57	Fen14
PG 2251+113	2139	Esp94
RBS 1121	4260 ± 1250	Min10
SBS 1116+583A	3950 ± 255	Fen14
Swift J2127.4+5654	2000	Mal08
TON 1388	2920 ± 80	Gru99
TON 1542	3470	San10
TON 1565	950^{+10}_{-0}	Sha07
Ton S180	1000	Ver01
UGC 3973	4735 ± 44	Fen14
UGC 6728	2308.3 ± 79.6	Win09
VII Zw 244	2899	Til13

Table A8. Recorded average white light continuum polarization of 100/124 AGNs. References: Mar83, Martin et al. (1983); Mil83, Miller & Antonucci (1983); Sch85, Schmidt & Miller (1985); Goo89, Goodrich (1989); Ber90, Berriman et al. (1990); Bri90, Brindle et al. (1990); Wil92, Wills et al. (1992); Kay94, Kay (1994); Tra95, Tran (1995); You96, Young et al. (1996); Bar99, Barth, Filippenko & Moran (1999); Kay99, Kay et al. (1999); Ogl99, Ogle et al. (1999); Ale00, Alexander et al. (2000); Mor00, Moran et al. (2000); Smi02, Smith et al. (2002); Sch03, Schmid et al. (2003); Lum04, Lumsden, Alexander & Hough (2004); Mor07, Moran (2007); Bat11, Batcheldor et al. (2011).

Object	Waveband (Å)	Pol. degree (per cent)	Pol. angle (°)	Reference
3C 120	3800–5600	0.92 ± 0.25	103.5 ± 7.9	Mar83
0019+0107	4000–8600	>0.98	35.0 ± 0.5	Ogl99
0145+0416	1960–2260	>2.14	126.0 ± 1.0	Ogl99
0226−1024	4000–8600	>1.81	167.1 ± 0.2	Ogl99
0842+3431	4000–8600	>0.51	27.1 ± 0.6	Ogl99
1235+1453	1600–1840	>0.75	175.0 ± 12.0	Ogl99
1333+2840	4000–8600	>4.67	161.5 ± 0.1	Ogl99
1413+1143	4000–8600	>1.52	55.7 ± 0.9	Ogl99
4C 13.41	3200–8600	0.94 ± 0.19	87.0 ± 6.0	Ber90
Akn 120	3800–5600	0.65 ± 0.13	78.6 ± 5.7	Mar83
Akn 564	6000–7500	0.52 ± 0.02	87.0 ± 1.3	Smi02
Circinus	5650–6800	22.4–25.0	45.0	Ale00
ESO 323–G077	3600	7.5	84	Sch03
Fairall 51	4700–7200	4.12 ± 0.03	141.2 ± 0.2	Smi02
Fairall 9	3800–5600	0.4 ± 0.11	2.4 ± 7.6	Mar83
I Zw1	3200–8600	0.61 ± 0.08	8.0 ± 3.0	Ber90
IC 4329A	5000–5800	5.80 ± 0.26	42.0 ± 1.0	Bri90
IC 5063	3800–5600	4.05–5.05	10.1 ± 3.2	Mar83
IRAS 13224–3809	4445–8150	0.38 ± 0.03	84.0 ± 2.0	Kay99
IRAS 13349+2438	3200–8320	23–35	124.0 ± 5.0	Wil92
K 348–7	3200–8600	0.25 ± 0.22	42.0 ± 25.0	Ber90
MCG–3–34–64	6015–7270	0.50 ± 0.20	75.0 ± 25.0	You96
MCG–6–30–15	5000–5800	4.06 ± 0.45	120.0 ± 3.0	Bri90
MCG+8–11–11	3800–5600	0.69 ± 0.46	166.4 ± 19.0	Mar83
Mrk 1014	3200–8600	1.37 ± 0.40	21.0 ± 8.0	Ber90
Mrk 1018	4180–6903	0.28 ± 0.05	165.1 ± 5.2	Goo89
Mrk 1066	3200–6200	>1.99	135.1 ± 2.6	Kay94
Mrk 110	3200–8600	0.17 ± 0.08	18.0 ± 15.0	Ber90
Mrk 1239	3800–5600	4.09 ± 0.14	136.0 ± 1.0	Mar83
Mrk 1298	3200–8600	0.32 ± 0.14	76.0 ± 12.0	Ber90
Mrk 1383	3200–8600	0.49 ± 0.19	58.0 ± 11.0	Ber90
Mrk 176	3800–5600	>0.54	146.3 ± 8.2	Mar83
Mrk 231	3800–5600	2.87 ± 0.08	95.1 ± 0.8	Mar83
Mrk 273	3800–5600	>0.37	66.7 ± 52.0	Mar83
Mrk 279	6000–7500	0.48 ± 0.04	58.9 ± 2.4	Smi02
Mrk 3	5000	7.77–8.61	167.0	Tra95
Mrk 304	3200–8600	0.58 ± 0.14	107.0 ± 7.0	Ber90
Mrk 335	3800–5600	0.48 ± 0.11	107.6 ± 6.9	Mar83
Mrk 34	3200–6200	>3.92	53.0 ± 4.5	Kay94
Mrk 348	3200–6200	>9.09	78.9 ± 1.3	Kay94
Mrk 359	4214–6937	0.46 ± 0.02	112.0 ± 1.2	Goo89
Mrk 463	3200–6200	>10	84.0	Tra95
Mrk 478	3800–5600	0.46 ± 0.15	44.9 ± 9.5	Mar83
Mrk 486	3800–5600	3.40 ± 0.14	136.8 ± 1.2	Mar83
Mrk 509	3800–5600	1.09 ± 0.15	146.5 ± 4.0	Mar83
Mrk 573	3200–6200	>5.56	48.0 ± 2.0	Kay94
Mrk 590	3800–5600	0.32 ± 0.30	105.9 ± 26.6	Mar83
Mrk 6	3800–5600	0.54 ± 0.15	141.2 ± 8.0	Mar83
Mrk 705	4700–7200	0.46 ± 0.07	49.3 ± 6.5	Smi02
Mrk 707	3800–5600	0.20 ± 0.24	140.9 ± 52.0	Mar83
Mrk 766	4500–7100	3.10 ± 0.80	90.0	Bat11
Mrk 78	3200–6200	21.0 ± 9.0	75.3 ± 11.2	Kay94
Mrk 79	3800–5600	0.34 ± 0.19	0.4 ± 16.2	Mar83
Mrk 841	4500–7500	1.00 ± 0.03	103.4 ± 1.0	Smi02
Mrk 876	3200–8600	0.50 ± 0.14	86.0 ± 8.0	Ber90
Mrk 877	3200–8600	0.95 ± 0.20	69.0 ± 6.0	Ber90
Mrk 896	3800–5600	0.55 ± 0.13	1.9 ± 7.1	Mar83

Table A8. – *continued*

Object	Waveband (Å)	Pol. degree (per cent)	Pol. angle (°)	Reference
NGC 1068	3500–5200	16.0 ± 2.0	95.0	Mil83
NGC 1097	5100–6100	0.26 ± 0.02	178 ± 2.0	Bar99
NGC 1320	3200–6300	>0.38	91.3 ± 3.0	Kay94
NGC 1365	5000–5900	0.91 ± 0.18	157 ± 6.0	Bri90
NGC 1386	3800–5600	>0.62	34.3 ± 7.1	Mar83
NGC 1566	3800–5600	0.60 ± 0.24	52.6 ± 11.6	Mar83
NGC 1667	5100–6100	0.35–9.8	94.0 ± 1.0	Bar99
NGC 2110	5200–6200	18.4	70.0	Mor07
NGC 2992	3800–5600	>3.32	33.3 ± 1.6	Mar83
NGC 3227	5000	1.3 ± 0.1	133 ± 3.0	Sch85
NGC 3516	4500–7500	0.15 ± 0.04	30.1 ± 8.0	Smi02
NGC 3783	4500–7500	0.52 ± 0.02	135.5 ± 1.0	Smi02
NGC 4051	4500–7500	0.55 ± 0.04	82.8 ± 1.8	Smi02
NGC 4151	4600–7400	0.26 ± 0.08	62.8 ± 8.4	Mar83
NGC 424	5000–5900	>1.53	59.0 ± 5.0	Kay94
NGC 4388	3800–5600	2.0–39.7	93.0 ± 29.0	Kay94
NGC 4395	5100–6100	0.64 ± 0.03	30.0 ± 2.0	Bar99
NGC 4507	5400–5600	14.8–16.3	37.0 ± 2.0	Mor00
NGC 4593	6000–7600	0.14 ± 0.05	109.5 ± 10.8	Smi02
NGC 5506	3200–6200	>2.6	72.8 ± 4.5	Kay94
NGC 5548	6000–7500	0.69 ± 0.01	33.2 ± 0.5	Smi02
NGC 5643	5000–5900	>0.75	57.0 ± 9.0	Bri90
NGC 7172	5000–5900	>2.10	96.0 ± 3.0	Bri90
NGC 7213	6000–7500	0.09 ± 0.02	146.0 ± 7.6	Smi02
NGC 7314	4500–7500	3.00 ± 1.00	35.0	Lum04
NGC 7469	6000–7500	0.18 ± 0.01	76.8 ± 1.7	Smi02
NGC 7582	3800–4900	>1.35	157 ± 5.0	Bri90
NGC 7674	3200–6200	6.54–7.6	31.0	Tra95
PG 0026+129	3200–8600	0.27 ± 0.17	83.0 ± 17.0	Ber90
PG 1001+054	3200–8600	0.77 ± 0.22	74.0 ± 8.0	Ber90
PG 1211+143	4700–7200	0.27 ± 0.04	137.7 ± 4.5	Smi02
PG 1244+026	3200–8600	0.48 ± 0.25	108.0 ± 15.0	Ber90
PG 1302–102	3200–8600	0.18 ± 0.15	26.0 ± 24.0	Ber90
PG 1411+442	3200–8600	0.76 ± 0.17	61.0 ± 6.0	Ber90
PG 1435–067	3200–8600	1.44 ± 0.29	27.0 ± 6.0	Ber90
PG 1448+273	3200–8600	0.27 ± 0.14	67.0 ± 15.0	Ber90
PG 1626+554	3200–8600	0.59 ± 0.19	10.0 ± 9.0	Ber90
PG 1700+518	3200–8600	0.54 ± 0.10	56.0 ± 5.0	Ber90
PG 2251+113	3200–8600	0.89 ± 0.22	50.0 ± 7.0	Ber90
TON 1388	3200–8600	0.23 ± 0.11	142.0 ± 13.0	Ber90
TON 1542	3200–8600	0.61 ± 0.12	118.0 ± 6.0	Ber90
TON 1565	3200–8600	0.31 ± 0.14	42.0 ± 13.0	Ber90
VII Zw244	3200–8600	1.08 ± 0.37	144.0 ± 10.0	Ber90

Table A9. Sublist from Table A8 of type 1 Seyfert galaxies exhibiting optical polarization spectra similar to those of type 2 objects (polar scattering dominated AGN).

Object	Pol. degree (per cent)
ESO 323–G077	7.5
Fairall 51	4.12 ± 0.03
Mrk 231	2.87 ± 0.08
Mrk 486	3.40 ± 0.14
Mrk 766	3.10 ± 0.80
Mrk 1239	4.09 ± 0.14
NGC 3227	1.3 ± 0.1
NGC 4593	0.14 ± 0.05
NGC 5548	0.69 ± 0.01

Table A10. Sublist from Table A8 of type 1 Seyfert galaxies exhibiting high (>2 per cent) optical polarization.

Object	Pol. degree (per cent)
ESO 323–G077	7.5
Fairall 51	4.12 ± 0.03
IC 4329A	5.80 ± 0.26
MCG–6–30–15	4.06 ± 0.45
Mrk 231	2.87 ± 0.08
Mrk 486	3.40 ± 0.14
Mrk 766	3.10 ± 0.80
Mrk 1239	4.09 ± 0.14
NGC 7314	3.00 ± 1.00

This paper has been typeset from a TEX/LATEX file prepared by the author.